Article

Impact of Polythiophene ((C₄H₄S)ₙ; n = 3, 5, 7, 9) Units on the Adsorption, Reactivity, and Photodegradation Mechanism of Tetracycline by Ti-Doped Graphene/Boron Nitride (Ti@GP_BN) Nanocomposite Materials: Insights from Computational Study

Daniel C. Agurokpon, Hitler Louis,* Innocent Benjamin, Obinna C. Godfrey, Suresh Ghotekar, and Adedapo S. Adeyinka*

Read Online

ACCESS | Metrics & More | Article Recommendations | Supporting Information

ABSTRACT: This study addresses the formidable persistence of tetracycline (TC) in the environment and its adverse impact on soil, water, and microbial ecosystems. To combat this issue, an innovative approach by varying polythiophene ((C₄H₄S)ₙ; n = 3, 5, 7, 9) units and the subsequent interaction with Ti-doped graphene/boron nitride (Ti@GP_BN) nanocomposites was applied as catalysts for investigating the molecular structure, adsorption, excitation analysis, and photodegradation mechanism of tetracycline within the framework of density functional theory (DFT) at the B3LYP-gd3bj/def2svp method. This study reveals a compelling correlation between the adsorption potential of the nanocomposites and their corresponding excitation behaviors, particularly notable in the fifth and seventh units of the polythiophene configuration. These units exhibit distinct excitation patterns, characterized by energy levels of 1.3406 and 924.81 nm wavelengths for the fifth unit and 1.3391 and 925.88 nm wavelengths for the seventh unit. Through exploring deeper, the examination of the exciton binding energy emerges as a pivotal factor, bolstering the outcomes derived from both UV−vis transition analysis and adsorption exploration. Notably, the calculated exciton binding energies of 0.120 and 0.103 eV for polythiophene units containing 5 and 7 segments, respectively, provide compelling confirmation of our findings. This convergence of data reinforces the integrity of our earlier analyses, enhancing our understanding of the intricate electronic and energetic interplay within these intricate systems. This study sheds light on the promising potential of the polythiophene/Ti-doped graphene/boron nitride nanocomposite as an efficient candidate for TC photodegradation, contributing to the advancement of sustainable environmental remediation strategies. This study was conducted theoretically; hence, experimental studies are needed to authenticate the use of the studied nanocomposites for degrading TC.
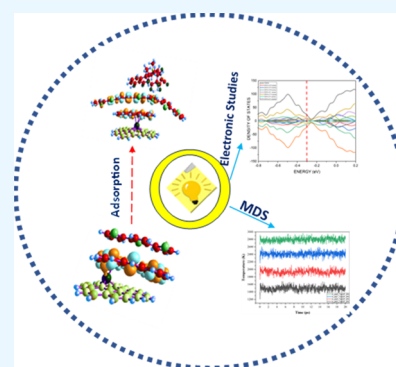
1. INTRODUCTION

The safe disposal of antibiotics has been a major concern to humans and pharmaceutical experts in particular because of their adverse effects on the environment.[1] This has lingered from the origin of antibiotic production because many environmental challenges continue to surface due to the residuals of antibiotics, which is among the causes of antimicrobial resistance over time.[2] Antibiotics, which are used for the treatment of bacterial infections, are based on a range of applications classified into narrow and broad spectrum. Narrow-spectrum antibiotics are designed to act upon a limited/targeted bacterial species, while broad-spectrum antibacterials have a wide range of application cutting across bacterial control in human and veterinary medicine.[3] Studies have reported that an antibiotic could not be totally digested and is therefore released to the environment,[4,5] hence causing adverse environmental contamination and multidrug resistance.

Tetracycline antibiotics comprising tetracycline, chlortetracycline, demeclocycline, and oxytetracycline are broad-spectrum antibiotics used for the management and treatment of infectious diseases. Semisynthetic tetracyclines include doxycycline lymecycline, methacycline, minocycline, and rolitetracycline including the recently reported groups such as ervacycline, omadacycline, and sarecycline.[6] These are widely used in human and veterinary medicine due to their broad-spectrum antibacterial activities and good therapeutic effects and are widely employed. However, due to its antibacterial properties and chemical durability, tetracycline (TC) is difficult to disintegrate spontaneously.[3] The residues
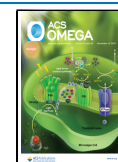
have been shown to limit the growth of microorganisms in soil and water as well as induce the development of antibiotic-resistance genes.[7,8]

The degradation of tetracycline has attracted many approaches due to challenging remedial difficulties. As a result, diverse approaches including bacteria,[9−11] pure culture fungi,[12−14] sludges,[15−20] adsorption,[21] electrochemistry,[22] hydrogen peroxide oxidation,[23,24] hydrolysis,[25−27] ozonation,[24] catalysis,[28−34] and so on have been employed by different researchers. However, effective degradation was not achieved in the cited studies. This has led to the current trend of applying nanotechnology in the degradation of TC by recent studies.[27−66] Studies on tetracycline degradation are almost inexhaustible in the literature, as a satisfactory degradation percentage is yet to be achieved. For instance, 66% mineralization of TC has been reported using $ZnWO_4$/Bi_2MoO_6 nanocomposites.[35] It has also been reported that TC is removed after 100 min through $UVC/MWCNT/TiO_2$ photocatalysis. Meanwhile, the researchers also reported that to obtain 83% mannerization, a longer period of about 300 min is required.[28] This challenge persists as the photocatalyst may cause secondary pollution.[1]

Having thoroughly explored the literature, several studies have used boron nitride,[67−82] graphene,[83−93] and titanium alongside other composites[94−102] to study the degradation of TC. However, no study was able to integrate polythiophene, titanium, graphene, and boron nitride as optimized in this study. Moreover, previous studies also failed to use polythiophene for the degradation of TC. The knowledge of the literature has also provided that studies applying titanium-doped graphene to degrade TC are very rare. At this point, there is a high conviction that the present study is unique and would contribute immensely to the literature, while it maximizes the challenges of TC degradation. Thus, poly-thiophene/Ti-doped graphene/boron nitride nanocomposites were considered theoretically to predict the photodegradation of TC for experimental studies. Boron nitride was used to enhance stability, while the titanium dopant was incorporated to improve[103,104] graphene reactivity with the polymer to adsorb TC components. Also, 3, 5, 7, and 9 polythiophene chains were considered to compare the effect of the polymers on other compounds. Herein, the binding energy, hole−electron, optical gap, exciton energy, UV transition, adsorption, and solvation were carefully studied to explain the photo-degradation of TC.

2. COMPUTATIONAL DETAILS

The electronic properties of the synthesized compounds were investigated using density functional theory (DFT), which is an electronic structural theory method.[105] The compound's structure was optimized using the B3LYP-gd3bj/def2svp method embedded in Gaussian16 software, and the geometry was visualized using GaussView 6.0.16 software.[103,104] The topological studies utilized to obtain additional insights into the deeper nature of interatomic interactions and to increase predictability of noncovalent interactions were quantum theory of atoms in molecules (QTAIM) and noncovalent interactions. Multiwfn 3.7 software developed by Lu et al.[106] was used to compute QTAIM and NCI. Using Multiwfn, a density of states (DOS) analysis was done to first understand the electronic distribution and then to view the fragment with the strongest contribution to the interactions between the studied nano-composites and TC. Visual molecular dynamics (VMD), a

molecular graphics program, was used to study the dipole moments created in the synthesized compounds by applying nonlinear optics (NLO), which is used to measure the magnitude of a dipole.

2.1. Molecular Dynamics Simulation Protocol. The Forcite Module on the Dassault Systèmes BIOVIA software program[105] was used to properly analyze the nature of the interaction between the adsorbate and the adsorbent. These dynamic variables were used in a Parallel 2 thread on a Windows system. We use the NVE ensemble, a virtual laboratory, that allows us to examine the behavior of our molecular structures over a simulated time of 1 ps, which is equivalent to 1000 steps, and an arbitrary number seed of around 1.6×10^8. The energy variables include a universal force field and charge. To add a touch of randomness and excitement, we equip our molecules with initial velocities that set their paths ablaze. Just like a sprinkle of stardust, we incorporate an arbitrary number seed of approximately 1.6×10^8 to ignite the magic of this molecular performance. Cubic spline truncation was employed for the atom-based summing of the van der Waals and electrostatic components with a cutoff distance of 12.5 A, spline width of 1 A, and buffer width of 0.5 A. The vivid visualizations of the picture of the molecular symphony that unfolded during our simulation were plotted by using the Origin plot.

3. RESULTS AND DISCUSSION

3.1. Optimization. Geometric optimization was carried out in this study to evaluate the changes in the bond length of the adsorbents and the adsorbate. The adsorbate (nano-composites) comprised three unique structures, which are polythiophene, boron nitride, and Ti-doped graphene. Four unique structures of the polymer (polythiophene) such as $(C_4H_2S)_n$ (n = 3, 5, 7, 9) were incorporated into the boron nitrate and Ti-doped graphene to form the adsorbent. The nanomaterials were thereafter optimized with the adsorbate (tetracycline) to form an interaction. This resulted in four systems, viz., tc_ptp3_Ti@GP_BN; tc_ptp5_Ti@GP_BN; tc_ptp7_Ti@GP_BN; and tc_ptp9_Ti@GP_BN. The geo-metric optimization in this study was conducted using the gd3bj/B3LYP at the def2svp level of theory. In the system tc_ptp3_Ti@GP_BN, the bond length of the dopant in the lattice of the graphene before optimization was observed as 1.851 1.851, and 1.856 Å for bond length Ti104−N25, Ti104−N26, and Ti104−N29, respectively, while the bond lengths after optimization were observed as 1.852, 1.851, and 1.856 for Ti104−N25, Ti104−N26, and Ti104−N29, respectively. In the system tc_ptp5_Ti@GP_BN, it was observed that Ti104−N25, Ti104−N26, and Ti104−N29 had their respective bond lengths of 1.852, 1.853, and 1.856 Å before interaction with a corresponding bond length of 1.852, 1.853, and 1.856 Å after optimization. The third system (tc_ptp7_Ti@GP_BN) possessed bond lengths of 1.851 1.853, and 1.856 Å before the interaction and 1.851, 1.853, and 1.856 Å after interactions for the bonds labeled Ti104−N25, Ti104−N26, and Ti104−N29, respectively, while the last interaction (tc_ptp9_Ti@GP_BN) possesses bond lengths of 1.851, 1.852, and 1.855 Å, for Ti104−N25, Ti104−N26, and Ti104−N29 bonds before the interaction with the respective bond lengths of 1.851, 1.851, and 1.855 Å. Overall, the bond lengths in all the system remain unchanged after optimization except for the Ti104−N25 bond of tc_ptp3_Ti@GP_BN with a slight shift from 1.851 to 1.852 Å. A negligible difference was also observed in

the Ti104−N26 bond of tc_ptp9_Ti@GP_BN with a slight shortage recorded after the interaction (1.852 to 1.851 A). This implies that the overall difference in the bond stability of all the systems both before and after interactions is negligible, suggesting that the electron stability is not highly influenced by the optimization. The geometric optimization results are presented in Table 1. Some previous studies, including Gber

Table 1. Geometric Parameters Before and After the Interaction of the Modeled Interfaces with Tetracycline (TC) at the DFT/B3LYP-gd3bj/def2svp Method

system	bond labels	interface	interactions
tc_ptp3_Ti@GP_BN	Ti104−N25	1.851	1.852
	Ti104−N26	1.851	1.851
	Ti104−N29	1.856	1.856
tc_ptp5_Ti@GP_BN	Ti104−N25	1.852	1.852
	Ti104−N26	1.853	1.853
	Ti104−N29	1.856	1.856
tc_ptp7_Ti@GP_BN	Ti104−N25	1.851	1.851
	Ti104−N26	1.853	1.853
	Ti104−N29	1.856	1.856
tc_ptp9_Ti@GP_BN	Ti104−N25	1.851	1.851
	Ti104−N26	1.852	1.851
	Ti104−N29	1.855	1.855

et al.,[107] have also reported similar geometric optimization results. The bond length observed in this study outshines some of the previous studies, especially those optimized with Ti. For example, Chen et al.[108] reported a bond length of 2.306 Å between the N atom and the Ti atom in their study. Another interesting perspective of this study is the insignificant increase in the bond lengths of the optimized compounds both before and after interacting with TC.

3.2. Molecular Dynamics (MD) Simulation. The adsorption capabilities of solid adsorbents and organic adsorbates may be studied using molecular dynamics (MD) modeling.[109] MD simulations are run on the nanocomposites to assess their tendency to adsorb on the TC surface.[110] This research was based on molecular dynamics (MD) simulations. The MD simulations are important for investigating the studied effect of the studied nanocomposites on TC adsorption.[101] MD simulations are a powerful computational method that uses quantum mechanical calculations in conjunction with classical molecular theory to model the behavior and characteristics of materials at the atomic scale.[111] According to the literature review, investigating MD simulations for adsorption and degradation is important because it gives basic insights, predicts material characteristics, and enables the rational design of effective sensing and detection of the researched TC.[112] The total energy of the system is a critical number in MD simulations that gives insights into the system's stability, bonding, and general behavior.[113] These simulations can highlight the energetics and dynamics of molecules interacting with nanocomposites, revealing binding strengths, optimal adsorption locations, and potential reaction routes.[114] According to the previous studies, a larger total energy might imply that the system is less stable,[115] which could imply that the atoms or molecules in the system are subjected to stronger repulsive forces, resulting in higher potential energy contributions.[116] It means that the system is susceptible to structural rearrangements, reactions, or other dynamical changes in order to relieve the excess energy.

This understanding is critical for developing effective nanocomposites for TC degradation. The results of the AIMD analysis are presented in Table 2. From the table, an increase in

Table 2. Summary of the Calculated Ab Initio Molecular Dynamic Simulation Analysis

parameters	initial	final	average ± std. dev
ptp3_Ti@GP_BN			
tot. energy (kcal/mol)	1353.957	1350.186	1351.221 ± 0.886
pot. energy (kcal/mol)	1242.922	741.010	771.053 ± 33.825
kin. energy (kcal/mol)	111.035	609.176	580.167 ± 33.346
temperature (K)	298.000	1634.929	1557.074 ± 89.494
ptp5_Ti@GP_BN			
tot. energy (kcal/mol)	1490.631	1487.996	1487.903 ± 0.879
pot. energy (kcal/mol)	1367.160	822.426	843.652 ± 32.914
kin. energy (kcal/mol)	123.471	665.570	644.251 ± 32.482
temperature (K)	298.000	1606.368	1554.915 ± 78.395
ptp7_Ti@GP_BN			
tot. energy (kcal/mol)	1634.603	1630.647	1631.402 ± 0.958
pot. energy (kcal/mol)	1498.696	876.779	919.265 ± 35.252
kin. energy (kcal/mol)	135.907	753.867	712.137 ± 34.771
temperature (K)	298.000	1652.988	1561.487 ± 76.241
ptp9_Ti@GP_BN			
tot. energy (kcal/mol)	1779.528	1778.015	1776.147 ± 1.006
pot. energy (kcal/mol)	1631.185	1064.149	1006.946 ± 36.868
kin. energy (kcal/mol)	148.343	713.866	769.201 ± 36.371
temperature (K)	298.000	1434.056	1545.217 ± 73.064
tc_ptp3_Ti@GP_BN			
tot. energy (kcal/mol)	1844.322	1836.846	1837.201 ± 1.128
pot. energy (kcal/mol)	1683.544	1028.244	1033.174 ± 36.932
kin. energy (kcal/mol)	160.779	808.602	804.027 ± 36.332
temperature (K)	298.000	1498.727	1490.247 ± 67.340
tc_ptp5_Ti@GP_BN			
tot. energy (kcal/mol)	1971.584	1964.792	1965.617 ± 1.147
pot. energy (kcal/mol)	1798.369	1089.219	1118.588 ± 38.374
kin. energy (kcal/mol)	173.215	875.573	847.028 ± 37.796
temperature (K)	298.000	1506.343	1457.235 ± 65.025
tc_ptp7_Ti@GP_BN			
tot. energy (kcal/mol)	2121.150	2114.034	2113.536 ± 1.204
pot. energy (kcal/mol)	1935.500	1198.278	1193.510 ± 39.395
kin. energy (kcal/mol)	185.651	915.756	920.026 ± 38.802
temperature (K)	298.000	1469.940	1476.794 ± 62.284
tc_ptp9_Ti@GP_BN			
tot. energy (kcal/mol)	2261.905	2254.140	2255.109 ± 1.190
pot. energy (kcal/mol)	2063.818	1251.642	1275.457 ± 41.772
kin. energy (kcal/mol)	198.086	1002.499	979.651 ± 41.162
temperature (K)	298.000	1508.152	1473.781 ± 61.923

the total energy for all of the studied systems was observed. After interacting with TC, there was a heralded increase in the systems such that the interaction with the least total energy (tc_ptp3_Ti@GP_BN: 1837.201 ± 1.128) was observed with total energy higher than the energy observed in the highest absorbent (ptp9_Ti@GP_BN: 1776.147 ± 1.006). Although the MD results are significant only when the before and after interactions are compared, it indicates that the total energy of the studied systems increases with an increase in the polythiophene chain, revealing that the system with the shortest chain is more stable and could be a better nanocomposite for the degradation of TC. However, temperature is an important parameter that must be considered before dismissing the stability of this study. High temperature is
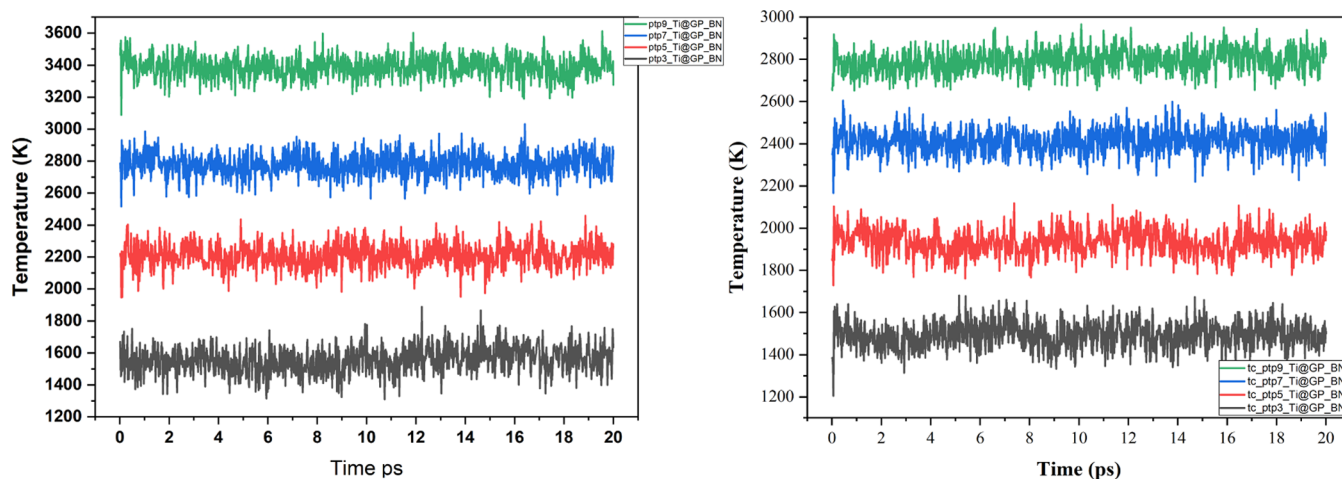
Figure 1. Pictorial projection of molecular dynamics (MD) simulations for the studied systems.

assumed to be associated with lower stability as high reactivity may lead to an increase in temperature. It is observed that tc_ptp3_Ti@GP_BN, tc_ptp5_Ti@GP_BN, tc_ptp7_Ti@GP_BN, and tc_ptp9_Ti@GP_BN have temperatures of 1498.727, 1506.343, 1469.940, and 1508.152 K, respectively. The temperatures observed across the four interactions studied do not significantly differ from each other, even though tc_ptp7_Ti@GP_BN is observed to require the least energy. This provides promising insights into the relevant properties of the 7-chain polythiophene nature concerning photodegradation. The pictorial representation of the molecular dynamic simulation is presented in Figure 1. In the figure, the dynamics of the studied systems were observed to be in agreement with the total energy.

3.3. Electronic properties. *3.3.1. Analysis of Density of States (DOS).* The density of states (DOS) is the number of various states that electrons may occupy within an atom at a certain energy level. This is the number of electron states per unit volume per unit energy and has a functional dependency on energy.[117] Total and partial densities of states (TDOS, OPDOS, and PDOS) were estimated to offer a more detailed description of the electronic properties. Also, DOS graphs are crucial tools for analyzing the nature and structure of electrons.[118] The PDOS and OPDOS curves are frequently used in the visual examination of orbital composition.[119] To determine the relative contributions of each atomic component, all the atoms which include H, N, B, C, Ti, S, and O of the studied compound were presented alongside their fragments in Figure 2a,b for the nanocomposites and interactions, respectively. As seen in the figure, an annotation key has been provided with colors corresponding to each of the fragments presented. Figure 2a entails the TDOS and PDOS of all the systems studied comprising four compounds for the nanocomposites and the remaining four for the interactions with tetracycline. From the graph, the highest contribution was made by the dopant (titanium) curve with a band gap range of −0.6 and −0.4 as seen in the highest occupied molecular orbital (HOMO), suggesting that the dopant contributes significantly to the stabilization of the studied compounds.

3.3.2. Band Gap Evolution (HOMO−LUMO). In the investigation of the band gap evolution, the frontier molecular orbital (FMO) analysis reveals a significant trend in the energy gaps of the nanocomposites. The nanocomposites, characterized by different polythiophene polymers (ptp5, ptp7, and

ptp9) interacting with Ti@GP_BN interfaces, exhibit a consistent pattern of decrease in their energy gaps. This gradual reduction in energy gaps from 1.931 to 1.732 eV signifies a systematic shift in the electronic structure. Upon the introduction of tetracycline, the energy gap alterations further accentuate this trend. The tetracycline-induced energy gap modifications for various systems, such as tc_ptp3_Ti@GP_BN, tc_ptp5_Ti@GP_BN, tc_ptp7_Ti@GP_BN, and tc_ptp9_Ti@GP_BN interactions, are captured and quantified. Interestingly, these interactions result in narrower energy gaps, with values of 1.907, 1.907, 1.808, and 1.733 eV, respectively. The decreasing order of energy gap reduction with increasing polythiophene polymer chain length is highlighted and tabulated in Table 3 for clarity. Comparing the energy gaps before and after tetracycline interactions provides a crucial perspective. The FMO analysis underscores that the nanocomposites exhibit higher energy gaps before interaction with tetracycline. This contrast is exemplified by the ptp3_Ti@GP_BN nanocomposite, where its energy gap decreases from 1.931 to 1.907 eV upon interaction with tetracycline. This computational evidence reinforces the idea that the presence of tetracycline instigates a stabilizing effect, leading to a decrease in the energy gap and suggesting a more stable reaction between the studied systems. The pictorial presentation of the flow of electrons from the HOMO to the lowest unoccupied molecular orbital (LUMO) is given in Figure 3. It is observable from the picture that the surfaces and the systems with the fifth, seventh, and ninth polythiophene units have great influence, which is evident from the HOMO to the LUMO isosurfaces.

3.3.3. Natural Bond Orbital (NBO) Analysis. The natural bond orbital (NBO) analysis was used to establish the nature of the donor−acceptor orbital connection that persisted between the nanocomposites. The NBO technique is a way for reducing the difficult Schrödinger equation to a simple chemical bonding idea that consumers can understand.[120] Furthermore, NBO analysis sheds information on the intermolecular charge transfer and electron delocalization that occurs between the adsorbed gases and the investigated nanocomposites.[121−123] In this work, NBO analysis was performed utilizing the gd3bj/B3LYP at the def2svp functional. The intensity of the interaction between the donor and acceptor orbitals is defined by the stabilization energy (E2). The greater the intensity of the donor−acceptor orbital
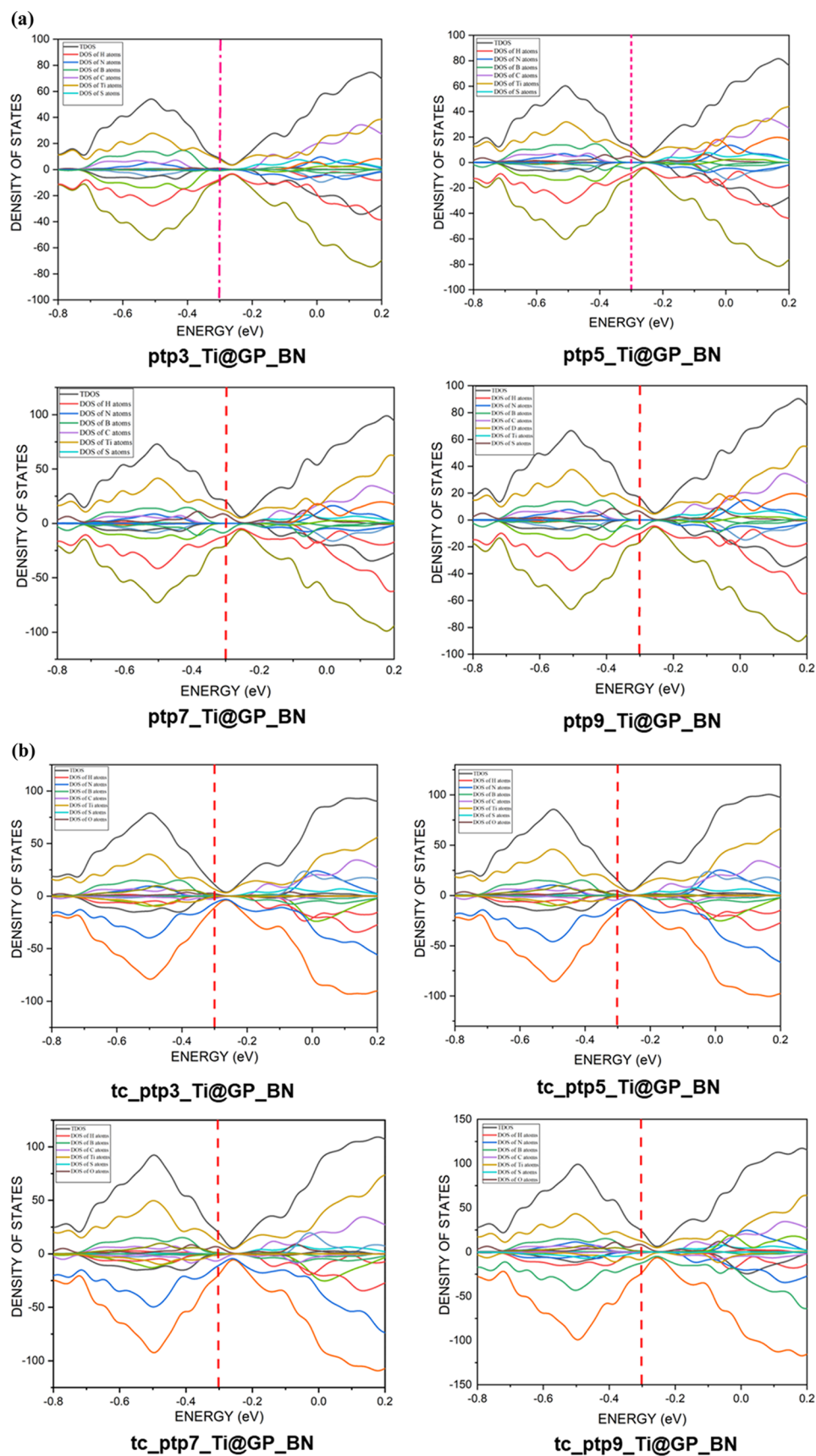
(a)

ptp3_Ti@GP_BN

ptp5_Ti@GP_BN

ptp7_Ti@GP_BN

ptp9_Ti@GP_BN

(b)

tc_ptp3_Ti@GP_BN

tc_ptp5_Ti@GP_BN

tc_ptp7_Ti@GP_BN

tc_ptp9_Ti@GP_BN

Figure 2. (a) Analysis of density of states (DOS) of the studied nanocomposites. (b) Analysis of density of states (DOS) of the studied nanocomposite interactions with antibiotics.

Table 3. HOMO−LUMO and Energy Gap/eV of the Systems Studied at the DFT/B3LYP-gd3bj/def2svp Method

systems	HOMO	LUMO	IP	EA	Eg
ptp3_Ti@GP_BN	−4.072	−2.141	4.072	2.141	1.931
ptp5_Ti@GP_BN	−4.065	−2.151	4.065	2.151	1.914
ptp7_Ti@GP_BN	−4.081	−2.253	4.081	2.253	1.828
ptp9_Ti@GP_BN	−4.093	−2.361	4.093	2.361	1.732
tc_ptp3_Ti@GP_BN	−4.027	−2.093	4.027	2.093	1.907
tc_ptp5_Ti@GP_BN	−3.999	−2.092	3.999	2.206	1.907
tc_ptp7_Ti@GP_BN	−4.014	−2.206	4.014	2.206	1.808
tc_ptp9_Ti@GP_BN	−3.985	−2.252	3.985	2.252	1.733

contact, the greater the value of the stabilization energy. The stabilization energy encountered by the donor−acceptor orbitals of the examined systems was determined in accordance with our earlier work.[124] Table S1 of the Supporting Information displays the stabilization energy constituting the most interacting donor−acceptor orbitals of the examined complexes. According to the tabulated results, all of the isolated nanocomposites and interactions exhibited the bonding donor−acceptor interaction of $\sigma \rightarrow \sigma^*$, the persisting

interaction $\pi \rightarrow \pi^*$, and the nonbonding interaction of LP $\rightarrow \sigma^*$. The ptp3_Ti@GP_BN nanocomposite has stabilization energies $E^{(2)}$ of 14.15, 41.15, and 581.50 kcal/mol for σN25−Ti104 $\rightarrow \sigma^*$N29−Ti104, πN18−B36 $\rightarrow \pi^*$N22−B35, and LpC79 $\rightarrow$ LpC64 bonding donor−acceptor orbitals, respectively. The ptp3_Ti@GP_BN nanocomposites possess stabilization energies of 14.34, 147.69, and 784.55 kcal/mol for σN25−Ti104 $\rightarrow \sigma^*$N29−Ti104, πC94−C97 $\rightarrow \pi^*$C93−C96, and LpC84 $\rightarrow$ Lp*C78 donor−acceptor orbitals, respectively. Similarly, the bonding donor−acceptor interactions of σN29−B48 $\rightarrow \sigma^*$TI104, πC62−C63 $\rightarrow \pi$S114, and LpC79 $\rightarrow$ LpC64 possess respective stabilization energies of 14.97, 83, and 727.09 for the ptp7_Ti@GP_BN nanocage. Also, ptp9_Ti@GP_BN has a stabilization energy of 14.5, 50.38, and 846.19 kcal/mol for σN29−B48 $\rightarrow \sigma^*$Ti104, πN23−B44 $\rightarrow \pi^*$B43, and LpC84 $\rightarrow$ Lp*C78 bonding donor−acceptor orbitals, respectively.

The NBO result for the intermolecular interaction (i.e., after interacting the tetracycline and nanocages) is presented as follows. The intermolecular system of tc_ptp3_Ti@GP_BN exhibited stabilization energies of 24.92, 50.13, and 795.35
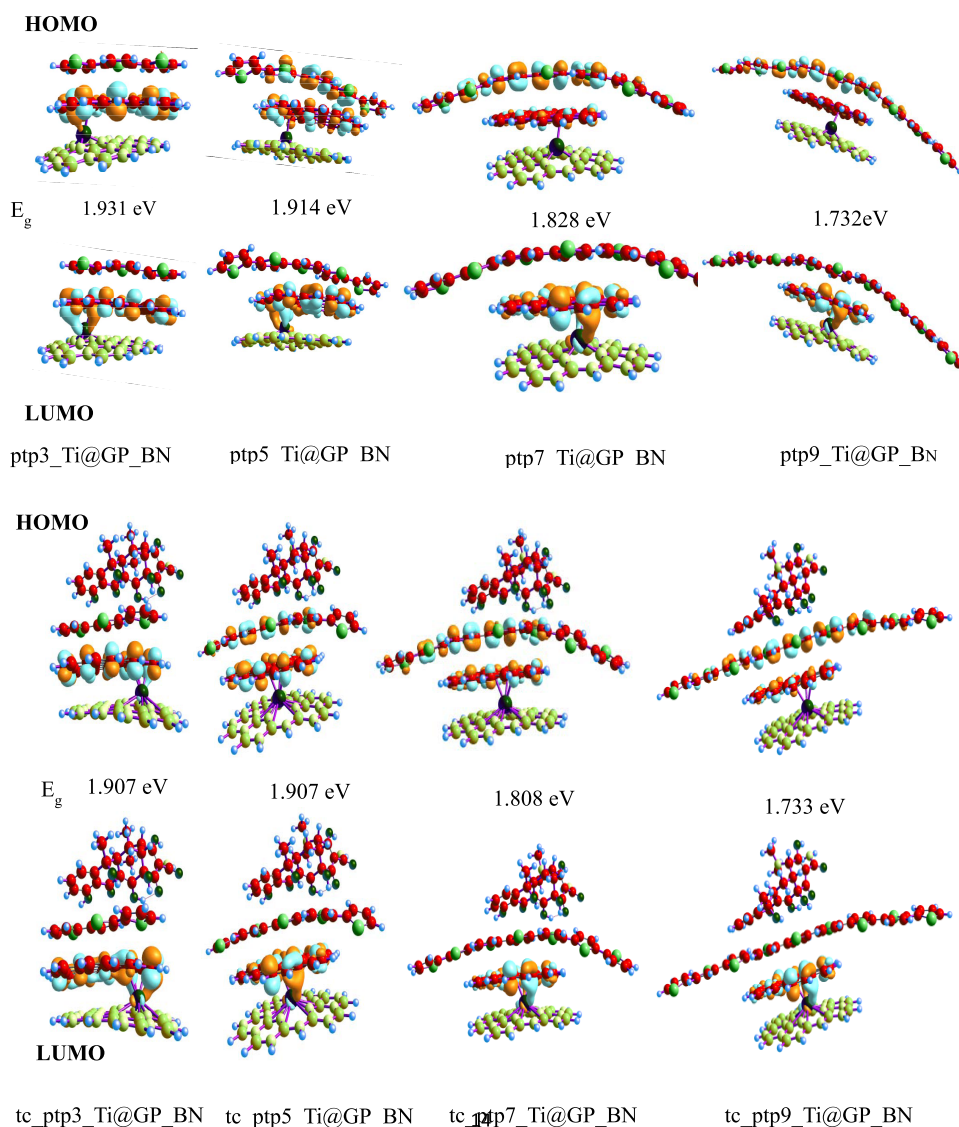
Figure 3. HOMO−LUMO isosurface of the studied system before and after the interaction.

kcal/mol for σ*N25−Ti104 → σ*Ti104, πN23−B44 → π*B43, and σC84 → σ*C78 bonding and acceptor orbitals, respectively. The second intermolecular system after interacting with tetracycline (tc_ptp5_Ti@GP_BN) exhibits stabilization energies of 26.21, 149.95, and 789.89 kcal/mol for the bonding donor−acceptor orbitals of σ*N25−Ti104 → σ*Ti104, π*C94−C97 → π*C93−C96, and σC84 → σ*C78, respectively. Also, stabilization energies of 22.81, 155.47, and 782.22 kcal/mol were observed for bonding donor−acceptor orbitals of σ*N29−Ti104 → σ*Ti104, π*C94−C97 → π*C93−C96, and σC84 → σ*C78, respectively, for the tc_ptp7_Ti@GP_BN intermolecular system. Furthermore, tc_ptp9_Ti@GP_BN, which is the last intermolecular system studied, exhibits bonding donor−acceptor orbitals of σ*N25−Ti104 → σ*Ti104, π*C126−C127 → π*C122−C124, and σC84σ*C78 with the respective stabilization energies of 26.17, 209.25, and 783.89 kcal/mol.

Comparatively, stabilization energies of the nanocomposites (ptp3_Ti@GP_BN, ptp5_Ti@GP_BN, ptp7_Ti@GP_BN, and ptp9_Ti@GP_BN) studied are relatively lower than their corresponding systems (tc_ptp3_Ti@GP_BN, tc_ptp5_Ti@GP_BN, tc_ptp7_Ti@GP_BN, and tc_ptp9_Ti@GP_BN) studied. For instance, the three bonding donor−acceptor orbitals of the first nanocomposites (ptp3_Ti@GP_BN) exhibit 14.15, 41.15, and 581.50 kcal/mol against the three bonds of the first system interacted (tc_ptp3_Ti@GP_BN) with energies of 24.92, 50.13, and 795.35 kcal/mol, which are comparably higher than the former. This can be applied to other nanocomposites and their corresponding systems. This implies that a positive interaction was achieved because higher stabilization energies after interacting the nanocomposites and the tetracycline signify a more stable compound. The result of this NBO analysis is slightly greater than the 783.89 kcal/mol reported by Mujafarkani et al.[125] compared to the 783.89 kcal/mol achieved for tc_ptp9_Ti@GP_BN in this study.

3.4. Topological Studies. *3.4.1. Quantum Theory of Atoms in Molecules (QTAIM).* The inter- and intramolecular bonding (hydrogen and non-hydrogen) interactions of the nanocomposites (polythiophene/Ti-doped graphene/boron nitride) and tetracycline are studied using quantum theory of atoms in molecules (QTAIM) as published by Bader and co-workers, which serve as a means of exploring the various kinds of interactions that exist in molecules. Furthermore, this approach tends to categorize bond gradient paths of electron density between atoms at bond critical locations,[126] and it is the primary instrument for characterizing atoms and bonds. Based on the localization of certain bond critical sites, the remarkable features of complexes and their orientation of molecules in real space may be examined.[127] The topological parameters such as density of all electrons $\rho(r)$, electron localization function (ELF), electronic charge density $V(r)$, electrophilicity index of electron density (ε), energy density $H(r)$, Hamiltonian kinetic energy $K(r)$, Lagrangian kinetic energy $G(r)$, Laplacian of electron density $\nabla^2\rho(r)$, and Eigen values of 1−3 (λ_1, λ_2, and λ_3) were calculated and are presented in Table S2. The nature of weak interactions can be examined from the results obtained from the calculation of $G(r)/V(r)$ and λ_1/λ_3. A cursory look at Table S2 reveals that the Laplacian of electron density $\nabla^2\rho(r)$ and the density of all electrons $\rho(r)$ values are positive and less than one ($\nabla^2\rho(r) < 1$ and $\rho(r) < 1$). In an attempt to classify the kinds of interactions present in each of the complexes, pairing systems

$\nabla^2\rho(r)$ and $H(r)$ were considered. Hence, when $\nabla^2\rho(r) \geq 0$ and $H(r) \geq 0$, it suggests a noncovalent interaction; however, when $\nabla^2\rho(r) \geq 0$ and $H(r) < 0$, it suggests a partial covalent interaction; also, when $\nabla^2\rho(r) < 0$ and $H(r) < 0$, it suggests a strong covalent bonding between the two bounded atoms.[128] The values of the electron density, $\rho(r)$, can be used to predict the strength of the interactions, of which a higher $\rho(r)$ value ($\rho > 0.1$ au) shows a stronger covalent interaction, while a lower $\rho(r)$ value ($\rho < 0.1$ au) indicates a weak noncovalent interaction.[129] In this study, all the $\rho(r)$ values for the interactions range from 0.326 to 0.901 au and are higher than 0.1, indicating the presence of strong bonding as observed in Table S2. The highest $\rho(r)$ value (0.901 au) was observed in O184−S114 of the tc_ptp7_Ti@GP_BN interaction, whereas the lowest $\rho(r)$ value (0.326 au) was recorded from O188−S121 of tc_ptp9_Ti@GP_BN interaction. Interestingly, the $\rho(r)$ values for all the bond paths are greater than 0.1 au, which signifies the complete presence of covalent bonding.

The Laplacian electron density $\nabla2\rho(r)$ as defined by the sum of the eigenvalues of Hessian (λ_1, λ_2, λ_3) provides an in-depth understanding on the electron density distribution. Previous studies have disclosed that positive values of $H(r)$ indicate the electrostatic nature of the interaction, while negative values signify the covalent nature.[130] As presented in Table S2, all interacting bonds were observed to be positive $H(r)$. BCPs with positive values for both Laplacian electron density ($\nabla2\rho(r) > 0$) and total electron energy density ($H(r) > 0$) are typical for closed-shell (noncovalent) interactions. However, a BCP with $H(r) < 0$ and $\nabla2\rho(r) < 0$ indicates a covalent interaction, while that with $H(r) < 0$ and $\nabla2\rho(r) > 0$ indicates a highly polar covalent interaction.[129] As reported in Table S2, all the bond paths, $\nabla2\rho(r)$, and $H(r)$ have positive values, indicating the total dominance of closed-shell interactions between the tetracycline and the nanocomposites. Furthermore, a small bond ellipticity ($\varepsilon < 1$) value at the BCPs indicates stable interactions.[129] In this study, there were only three CBPs: O191−H138 for tc_ptp5_Ti@GP_BN, O205−H137 for tc_ptp7_Ti@GP_BN, and O188−S121 for tc_ptp9_Ti@GP_BN showed stability with ε of 0.063, 0.061, and −0.138, respectively. Other CBPs were observed to be unstable with ε values ranging from 0.141 to 1.043 for all tc_ptp3_Ti@GP_BN bonds, 0.442 to 9.687 for tc_ptp5_Ti@GP_BN, 0.858 to 1.340 for tc_ptp3_Ti@GP_BN, and 0.563 to 4.125 for tc_ptp9_Ti@GP_BN.

Additionally, $G(r)/V(r) \geq 1$ confirms that the type of the chemical bond interaction is noncovalent (closed shell) in nature, while the covalent (shared) interaction is prominent when $G(r)/V(r) < 0.5$. Similarly, a partially covalent interaction is prevalent when $G(r)/V(r)$ is between 0.5 and 1. In this study, only two BCPs were observed with $G(r)/V(r) \geq 1$.[131] Unless for the first two bond paths of the first compound in Table S2, the $G(r)/V(r)$ was dominated by negative values, suggesting the dominance of shared interactions. The electron localization function (ELF) is critical in determining the strength of a covalent bond. When the ELF value is between 0.5 and 1, it indicates that there are bonding and nonbonding localized electrons in the area. The electron is delocalized when the ELF value is less than 0.5.[132] In this study, only all of the ELF values were lower than 0.5, suggesting a delocalization of electrons of the compounds.

3.4.2. Noncovalent Interactions (NCI). In addition to QTAIM, the NCI was characterized to re-examine the nature of the "closed-shell" noncovalent forces in the interactions
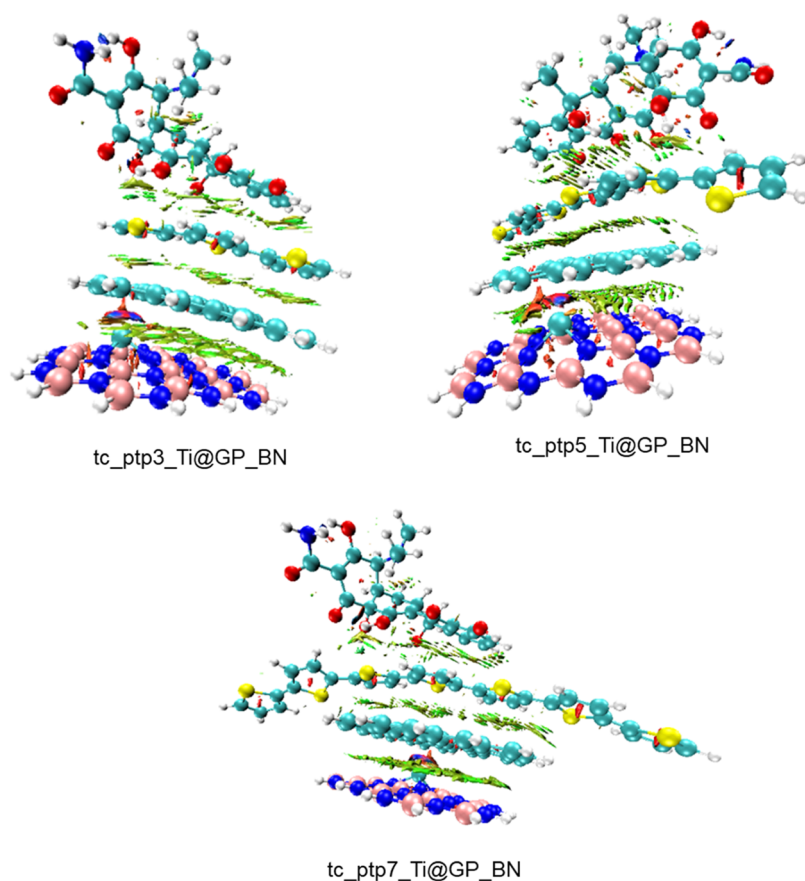
tc_ptp3_Ti@GP_BN

tc_ptp5_Ti@GP_BN

tc_ptp7_Ti@GP_BN

Figure 4. Pictorial representation of the reduced density gradient (RDG) of the studied system.

Table 4. Projected Adsorption Study of the Investigated Systems at the DFT/B3LYP-gd3bj/def2svp Method

systems	Ecomplx	Esurf	tetracycline	Ead	eV
tc_ptp3_Ti@GP_BN	−6959.89	−5396.79	−1562.47	−0.62816	−17.0931
tc_ptp5_Ti@GP_BN	−8063.14	−6500.04	−1562.47	−0.63269	−17.2165
tc_ptp7_Ti@GP_BN	−9166.39	−7603.29	−1562.47	−0.63272	−17.2171
tc_ptp9_Ti@GP_BN	−10269.6	−8706.53	−1562.47	−0.62908	−17.1181

within the studied compounds, especially at the point where the Ti dopant is. Herein, Multiwfn software[133] was used to study the noncovalent bonds. The noncovalent interaction emanates through a number of different mechanisms such as the van der Waals interactions, hydrogen bonding, and electrostatic interactions. The second density Hessian eigenvalue $\lambda(r)$, the electron density $r(r)$, and reduced density gradient (RDG) are the basic functions present in NCI analysis for the prediction of weak interactions. Surface plots involving the two functions give information about the type of weak interaction present. In the surface plot, the reduced density gradient (RDG) is plotted against the second eigenvalue of the electron density Hessian matrix (λ_2) and the electron density $r(r)$, that is, the NCI graph is a graph of RDG against $\lambda_2(r)r(r)$. From the surface, the nature of the weak interaction can be characterized depending on the values of λ_2. The blue region with negative values, $\lambda_2(r)r(r) < 0$, corresponds to strong interactions (such as hydrogen bonding) and high electron density, while the red region with positive values ($\lambda2(r)r(r) \geq 0$) indicates a strong repulsive interaction (like steric effect) and electron density depletion; the green region (sign l2(r)r(r) z 0) corresponds to relatively weak van der Waal interactions.[123,134] As evident from the plots in Figure 4, the

blue regions existing around the dopant (Ti) indicate the presence of strong bonding between doped graphene and boron nitrite. The green region observed between all the complexes indicates that van der Waals forces play a key role in the interaction of the complexes. In addition, little repulsion interaction is observed during the adsorption process. These are in good agreement with the DOS and QTAIM results.

3.5. Adsorption Studies. Different orientations of tetracycline on nanocomposites were studied in order to acquire the most stable adsorption configuration. All minimal energy complexes were computed by using gd3bj/B3LYP at the def2svp level. The adsorption energy may be used to determine how efficiently tetracycline is absorbed by an adsorbent.[135] The more the negative value of adsorption energy, the stronger the structure after adsorption.[136,137] From the results in the table, it was observed that all systems possess the chemosorption type of adsorption based on the negative enthalpy of adsorption with energies ranging between −17.0931 and −17.2171 eV. It was also observed that the differences in the adsorption energies of all the systems are relatively negligible even though tc_ptp7_Ti@GP_BN (−17.2171 eV) and tc_ptp5_Ti@GP_BN (−17.2165 eV) exhibited the highest energies as presented in Table 4. This

Table 5. Excitation State, Wavelength of Absorption, Oscillator Strength, and % Contribution with Assignment of the Studied Systems at the TD-DFT/B3LYP-gd3bj/def2svp Method

parameters	excited state	energy (eV)	wavelength absorption/λmax (nm)	oscillator strength (f)	contribution (%)	assignment
ptp3_Ti@GP/BN	S0→S1	1.3703	904.81	0.0061	310 → 312 (56.439)	$\pi \to \pi^*$
	S0→S2	1.5651	792.18	0.0759	310 → 311 (51.112)	$\pi \to \pi^*$
	S0→S3	1.7804	696.37	0.0164	310 → 313 (68.623)	$\pi \to \pi^*$
ptp5_Ti@GP/BN	S0→S1	1.3515	917.36	0.0072	352 → 353 (50.367)	$\pi \to \pi^*$
	S0→S2	1.5503	799.73	0.0447	352 → 354 (35.436)	$\pi \to \pi^*$
	S0→S3	1.5714	788.98	0.0395	352 → 354 (62.514)	$\pi \to \pi^*$
ptp9_Ti@GP/BN	S0→S1	1.3248	935.90	0.0139	436 → 437 (78.518)	$\pi \to \pi^*$
	S0→S2	1.3680	906.34	0.0076	436 → 440 (39.534)	$\pi \to \pi^*$
	S0→S3	1.5657	791.87	0.0654	436 → 438 (44.676)	$\pi \to \pi^*$
tc_ptp3_Ti@GP/BN	S0→S1	1.3878	893.41	0.0070	427 → 429 (59.599)	$\pi \to \pi^*$
	S0→S2	1.5658	791.81	0.0763	427 → 428 (54.230)	$\pi \to \pi^*$
	S0→S3	1.797	689.97	0.0155	427 → 432 (54.913)	$\pi \to \pi^*$
tc_ptp5_Ti@GP/BN	S0→S1	1.3406	924.81	0.0075	469 → 470 (52.695)	$\pi \to \pi^*$
	S0→S2	1.524	813.54	0.0384	469 → 471 (62.070)	$\pi \to \pi^*$
	S0→S3	1.566	791.71	0.0486	469 → 471 (36.611)	$\pi \to \pi^*$
tc_ptp7_Ti@GP/BN	S0→S1	1.3391	925.88	0.0109	511 → 515 (39.071)	$\pi \to \pi^*$
	S0→S2	1.395	888.79	0.0137	511 → 512 (75.299)	$\pi \to \pi^*$
	S0→S3	1.5646	792.46	0.0652	511 → 515 (44.666)	$\pi \to \pi^*$
tc_ptp9_Ti@GP/BN	S0→S1	1.3441	922.43	0.0273	553 → 554 (58.976)	$\pi \to \pi^*$
	S0→S2	1.377	900.37	0.0182	553 → 554 (39.379)	$\pi \to \pi^*$
	S0→S3	1.5561	796.78	0.0657	553 → 555 (46.991)	$\pi \to \pi^*$

suggests strong and irreversible adsorption, implying that the studied nanocomposites are compatible and could be used for the degradation of tetracycline in the environment because the higher the adsorption energy, the more the sensing ability of a nanomaterial.[138−140]

According to adsorption theory by Dąbrowski,[141] as the temperature rises, the likelihood of molecules sticking to a material's surface weakens due to increased thermal energy, leading to reduced adsorption. Higher temperatures facilitate molecule detachment from the surface and favor fluid-phase interactions, altering the adsorption equilibrium.[142] Although these studied systems are in the ground state, which may not accurately estimate the temperature and time exerted for the studied nanocomposites to degrade TC, this study hypothesize lower temperature in tc_ptp5_Ti@GP_BN and tc_ptp7_Ti@GP_BN interactions compared to tc_ptp3_Ti@GP_BN and tc_ptp9_Ti@GP_BN. This is explained by the high adsorption energy observed in the studied interactions.

This result is insightful, as many studies have reported weaker adsorption potentials. Yang et al.[143] reported an adsorption energy of −9.39 eV after studying the oxygen-containing functional groups on formaldehyde adsorption in a solution on the carbon surface. The highest adsorption energy was reported by Guo et al.[144] as −5.83 eV, observed in the literature related to the photodegradation of organic pollutants, which is significantly lower compared to the adsorption result obtained in the present study. Based on TC photodegradation, Meng et al.[145] reported an adsorption energy of −2.17 eV after using Fe@MoS$_2$ as a piezocatalyst for the durable degradation of tetracycline. Additionally, Liu et al. reported an adsorption energy of −2.56 eV after utilizing Fe$_3$O$_4$@CNT as a catalyst for tetracycline degradation in peroxydisulfate. There seems to be a similar trend in the literature regarding the highest reported adsorption energies. This is confirmable by Bahamon et al., which reported −2.9 eV adsorption energy after studying the electronic interactions of an SO$_2$ molecule on a CoP hydrotreating catalyst. This provides commendable computa-

tional evidence that the nanocomposites used in this study for the photodegradation of TC are insightful materials.

3.6. Photodegradation. *3.6.1. UV Transition.* To comprehend and clearly explain the different kinds of electronic excitation (rotational and vibrational modes) in the investigated compound, UV−Vis spectroscopic study has been obtained using the gd3bj/B3LYP at the def2svp level of theory.[118,146] Table 5 shows the theoretical results for oscillator strength (f value), energy of excitation (E), percent contribution, and potential assignments carried out in the different compounds studied. From Table 5, the result showed that all phases of orbitals 136−140 exhibit an excited-state transition from S0 to S1, S2, and S3 with an assignment of $\pi \to \pi^*$ (pi orbitals to the antibonding orbital). This study compared the parameters of the nanomaterials before and after interacting with tetracycline antibiotics. It was observed that the energy (eV) of all the compounds increases with an increase in the excitation, leaving the excitation from S0 to S1 with the least energies in all the compounds (both before and after the interaction). The energy observed in all the excited states of the studied compounds ranged between 1.3248 and 1.7970 eV. Although exceptions were observed, the before and after interaction comparison revealed that the energy of the studied parameters decreases after interacting with tetracycline, suggesting a more adsorption stability of the compound investigated. It was also observed that the wavelength absorption/λmax (nm) values decrease with increased excitation states across all studied parameters.

As presented in Table 5, the interaction with the shortest polythiophene unit (tc_ptp3_Ti@GP/BN) was observed with the highest UV excitation energy of 1.3878 eV followed by tc_ptp5_Ti@GP/BN (1.3406 eV) and tc_ptp9_Ti@GP/BN (1.3441 eV), and last, the interaction with seven polythiophene units (tc_ptp7_Ti@GP/BN) was observed with the smallest excitation energy of 1.3391 eV, revealing the most stability-influencing unit for the degradation of TC. The wavelength presented in Table 5 also presents insightful information about

the photodegradation of TC. Herein, longer wavelengths account for higher photodegradation potentials. It was observed that the TC interaction with the 3-chain polythiophene unit has the shortest adsorption wavelength (893.41 nm) followed by the 9-units (922.43 nm), the 5-units (924.81 nm), and the 7-chain polythiophene units (925.88 nm). The wavelength results closely aligned with the results of the excitation energy, revealing that interactions with lower excitation account for longer wavelengths aligning with already established facts in the literature. This suggests that the 7-unit polythiophene has the highest influence closely followed by the 5-unit polythiophene on the nanocomposites for the photodegradation of TC. Previous studies reported the wavelength and excitation energy: 460.35 nm and 2.6933 eV by Udoikono et al.;[147] 249.90 nm and 4.96 eV by Owen et al.;[148] and 502.57 nm and 2.4670 eV by Apebende et al.; these are low compared to the present study. This explains that the nanocomposites as influenced by the polythiophene units are promising materials for the photodegradation of TC compared to the cited studies. The percentage contribution of all the orbitals is reported in the table with percentage values between 35.436 and 78.518% among all of the parameters. The transition wavelength of the various studied interactions is presented pictorially in the UV spectral as shown in Figure 5.
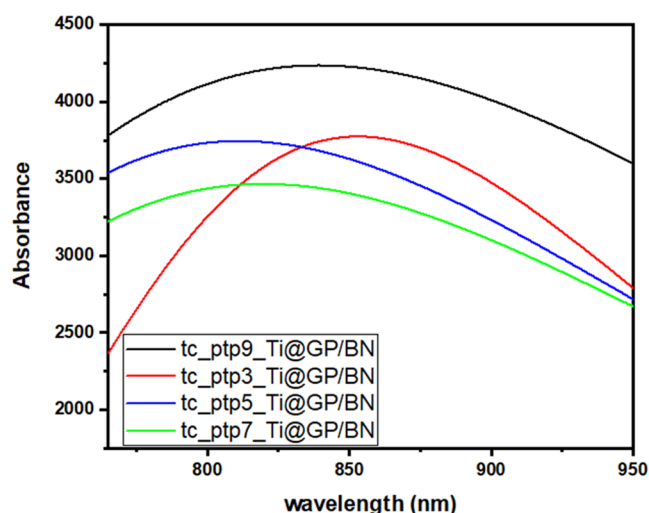

Figure 5. UV−vis transition spectra showing the transition wavelength of the studied interactions.

3.6.2. Hole−Electron, Optical Gap, Exciton Energy. This analysis was conducted to understand how the arrangement of polythiophene units impacts the stability and efficiency of Ti-doped graphene/boron nitride nanocomposites in degrading tetracycline through photocatalysis. Herein, the excitation binding energy (E_b) is used to determine the hole and the electron separation potential, which tells the stability of the studied compounds with respect to TC degradation. The exciton binding energy is the energy required to separate an exciton from its bound electron and hole partners. It is an intriguing parameter for the investigation of the photocatalytic characteristics, exciton dissociation potential, and efficacy of the nanocomposites.[149] A higher exciton system indicates more stability and hence provides insights into the durability of the degradation. E_b is determined as the difference between the HOMO−LUMO energy gap and E_{opt} (first excitation energy, as presented in the UV section). With the help of E_b, the

interaction of the coulombic forces between the hole and electron is calculated. The E_b of the compounds is calculated by using eq 1

$$E_b = E_{H-L} - E_{opt} \tag{1}$$

Here, E_{H-L} shows the band gap of the interaction at their excited state and E_{opt} represents the minimal energy required for the first excitation (S0−S1), also known as the first singlet excitation energy produced by pairing the hole and electron.[150] A lower value of E_b is correlated with a weaker electron−hole interaction.[151] As demonstrated in Table 6, the investigated

Table 6. Calculated E_{L-H} and E_{opt} of the Studied Interactions at the TD-DFT/B3LYP-gd3bj/def2svp Method

compounds	E_{H-L}	E_{opt}	E_b
tc_ptp3_Ti@GP_BN	1.493090	1.3878	0.105290
tc_ptp5_Ti@GP_BN	1.460708	1.3406	0.120108
tc_ptp7_Ti@GP_BN	1.441932	1.3391	0.102832
tc_ptp9_Ti@GP_BN	1.425877	1.3441	0.081777

compounds exhibit a discernible trend of decreasing exciton energy, arranged as tc_ptp5_Ti@GP_BN ≥ tc_ptp3_Ti@GP_BN ≥ tc_ptp7_Ti@GP_BN ≥ tc_ptp9_Ti@GP_BN, accompanied by the corresponding E_b values of 0.120108 ≥ 0.105290 ≥ 0.102832 ≥ 0.081777 eV. Notably, the first three compounds share proximity in terms of exciton energy, differing from the compound housing the longest polythiophene unit, which displays lower exciton energy. Among these, the interaction involving the 5-chain polythiophene unit attains the highest exciton binding energy of 0.120108 eV, aligning seamlessly with the UV−vis transition analysis and adsorption studies expounded upon in the preceding sections. This observed range of exciton binding energies resonates with prior investigations exploring the diverse landscape of exciton binding energies in relation to various semiconductors. In the context of this study, the deliberate incorporation of polythiophene, an organic semiconductor into the Ti-doped graphene/boron nitride nanocomposite, serves as a catalyst for the photodegradation of TC, an organic pollutant. Remarkably, the scope of exciton binding energies identified within this study remains consistent with the established range of 0.1−1.0 eV for organic semiconductors.[152] However, the outlier, tc_ptp9_Ti@GP_BN, featuring the longest polythiophene unit, deviates from the anticipated pattern, showcasing inconsistency with the established range.

This result aligns with certain previous studies that explored similar electron−hole properties through exciton binding energy analysis. For instance, Aldrich et al. reported the highest exciton binding energy of 0.11 eV,[153] which is approximately in line with the results obtained from this study. Notably, some previous studies reported lower optical gaps. For instance, Hao et al. reported the highest exciton binding energy of 0.07 eV reported by Hao et al.,[154] which is significantly lower compared to the findings of the present study. The present study demonstrates strong electron−hole properties compared to Wang et al.,[155] which reported the highest exciton binding energy of 0.10 eV. The differences observed between the present and the cited study could have resulted from the different nanocomposites studied. This provides tangible evidence that the nanocomposites could be excellent materials for the removal of TC through photodegradation. The outcomes gleaned from this comprehensive

exciton analysis strongly suggest that the initial three polythiophene units harbor the significant potential for driving insightful degradation properties, corroborated by their observable impact on hole−electron stability.

4. CONCLUSIONS

Considering the intricate challenges surrounding the secure disposal of antibiotics, an issue of profound concern for both the general public and pharmaceutical experts alike, the imperative to devise effective mitigation strategies becomes evident. Thus, the significance of this research resides in its pursuit of elucidating the distinct influence of polythiophene units on the photodegradation of tetracycline, specifically in the context of Ti-doped graphene/boron nitride nano-composite materials. This inquiry, executed within the purview of density functional theory (DFT) employing the gd3bj/B3LYP functional with a def2svp basis set, endeavors to unveil previously uncharted molecular-level interactions and mecha-nisms. This pursuit engenders a heightened comprehension of the intricate interplay between the nanocomposite's architec-ture and its capacity to facilitate the photodegradation of tetracycline through photoinduced processes. The investiga-tion into adsorption energies within various systems yielded intriguing findings, revealing remarkably minor disparities among the observed adsorption energies. Notably, tc_ptp7_Ti@GP_BN (−17.2171 eV) and tc_ptp5_Ti@GP_BN (−17.2165 eV) emerged as the frontrunners in terms of energy levels despite the marginal discrepancies. These outcomes prompt a deeper exploration of the underlying factors at play.

Upon closer scrutiny through UV−vis transition analysis, an intriguing correlation emerged between the adsorption potential of the systems and their corresponding excitation behaviors. Specifically, the fifth and seventh units of the polythiophene configuration displayed distinctive patterns of excitation, characterized by energy levels of 1.3406 and 1.3391 eV, accompanied by the corresponding wavelengths of 924.81 and 925.88 nm, respectively. This alignment between excitation properties and adsorption potential adds a layer of complexity to our understanding, suggesting an intricate interplay between electronic transitions and surface inter-actions. Delving further into the intricacies of the studied systems, the examination of exciton binding energy emerges as a pivotal component in fortifying the outcomes from both UV−vis transition analysis and adsorption investigation. Impressively, the calculated exciton binding energies of 0.120 and 0.103 eV for polythiophene units containing 5 and 7 segments, respectively, provide compelling corroborative evidence. This convergence of data reaffirms the validity of earlier UV−vis transition analysis and adsorption exploration, consolidating our grasp of the electronic and energetic dynamics at play within these complex systems.

ASSOCIATED CONTENT

Data Availability Statement

All data are contained within the article and electronic Supporting Information (ESI).

Ⓢ Supporting Information

The Supporting Information is available free of charge at https://pubs.acs.org/doi/10.1021/acsomega.3c04625.

Natural bond orbital analysis and quantum theory of atoms in molecules (PDF)

AUTHOR INFORMATION

Corresponding Authors

Hitler Louis − *Computational and Bio-Simulation Research Group, University of Calabar, Calabar 540221, Nigeria; Department of Pure and Applied Chemistry, University of Calabar, Calabar 540221, Nigeria; Centre for Herbal Pharmacology and Environmental Sustainability, Chettinad Hospital and Research Institute, Chettinad Academy of Research and Education, Kelambakkam 603103 Tamil Nadu, India;* ● orcid.org/0000-0002-0286-2865; Email: louismuzong@gmail.com

Adedapo S. Adeyinka − *Department of Chemical Sciences, University of Johannesburg, Auckland Park 2006, South-Africa;* Email: aadeyinka@uj.ac.za

Authors

Daniel C. Agurokpon − *Computational and Bio-Simulation Research Group, University of Calabar, Calabar 540221, Nigeria;* ● orcid.org/0000-0002-4609-9849

Innocent Benjamin − *Computational and Bio-Simulation Research Group, University of Calabar, Calabar 540221, Nigeria;* ● orcid.org/0000-0002-3514-5758

Obinna C. Godfrey − *Computational and Bio-Simulation Research Group, University of Calabar, Calabar 540221, Nigeria; Department of Biochemistry, University of Calabar, Calabar 540221, Nigeria;* ● orcid.org/0000-0002-3868-4028

Suresh Ghotekar − *Department of Chemistry, Smt. Devkiba Mohansinhji, Chauhan College of Commerce and Science, University of Mumbai, Silvassa 396, India;* ● orcid.org/0000-0001-7679-8344

Complete contact information is available at:
https://pubs.acs.org/10.1021/acsomega.3c04625

Author Contributions

H.L.: project conceptualization, design, and supervision. I.B. and D.C.A.: writing, result extraction, analysis, and article first draft. S.G. and O.G.: investigation. A.A.: resources and software.

Notes

The authors declare no competing financial interest.

REFERENCES

(1) Shao, S.; Wu, X. Microbial degradation of tetracycline in the aquatic environment: a review. *Crit. Rev. Biotechnol.* **2020**, *40* (7), 1010−1018.

(2) Ekpiken, E. S.; Agurokpon, D. C.; Ekah, D. F. Antibiotic Resistance of enteric bacterial pathogens in Accident and Emergency Units of Selected Public Hospitals in Calabar Metropolis, Cross River State. *Int. J. Curr. Res. Med.* **2023**, *9* (1), 1−13.

(3) Gaballah, M. S.; Li, X.; Zhang, Z.; et al. Determination of tetracycline, oxytetracycline, sulfadiazine, norfloxacin, and enroflox-acin in swine manure using a coupled method of on-line solid-phase extraction with the uhplc−dad. *Antibiotics* **2021**, *10* (11), 1397.

(4) Chang, D.; Mao, Y.; Qiu, W.; Wu, Y.; Cai, B. The Source and Distribution of Tetracycline Antibiotics in China: A Review. *Toxics* **2023**, *11* (3), 214.

(5) Xia, C.; Joo, S. W.; Hojjati-Najafabadi, A.; et al. Latest advances in layered covalent organic frameworks for water and wastewater treatment. *Chemosphere* **2023**, *329*, No. 138580.

(6) Mouton, J. W.Neomycin. In *Kucers' The Use of Antibiotics Sixth Edition*; CRC Press, 2010; pp 742−747. DOI: 10.1201/9781315152110.

(7) Hou, J.; Wang, C.; Mao, D.; Luo, Y. The occurrence and fate of tetracyclines in two pharmaceutical wastewater treatment plants of Northern China. *Environ. Sci. Pollut. Res.* **2016**, *23* (2), 1722−1731.

(8) Sanganyado, E.; Gwenzi, W. Antibiotic resistance in drinking water systems: Occurrence, removal, and human health risks. *Sci. Total Environ.* **2019**, *669*, 785−797.

(9) Wu, G. R.; Sun, L. J.; Xu, J. K.; Gao, S. Q.; Tan, X. S.; Lin, Y. W. Efficient Degradation of Tetracycline Antibiotics by Engineered Myoglobin with High Peroxidase Activity. *Molecules* **2022**, *27* (24), 8660.

(10) Al-Dhabi, N. A.; Esmail, G. A.; Valan Arasu, M. Effective degradation of tetracycline by manganese peroxidase producing Bacillus velezensis strain Al-Dhabi 140 from Saudi Arabia using fibrous-bed reactor. *Chemosphere* **2021**, *268*, No. 128726.

(11) Yin, Z.; Xia, D.; Shen, M.; et al. Tetracycline degradation by Klebsiella sp. strain TR5: Proposed degradation pathway and possible genes involved. *Chemosphere* **2020**, *253*, No. 126729.

(12) Yang, J.; Lin, Y.; Yang, X.; Ng, T. B.; Ye, X.; Lin, J. Degradation of tetracycline by immobilized laccase and the proposed transformation pathway. *J. Hazard Mater.* **2017**, *322*, 525−531.

(13) Tan, H.; Kong, D.; Ma, Q.; et al. Biodegradation of Tetracycline Antibiotics by the Yeast Strain Cutaneotrichosporon dermatis M503. *Microorganisms* **2022**, *10* (3), 565.

(14) Wen, X.; Jia, Y.; Li, J. Degradation of tetracycline and oxytetracycline by crude lignin peroxidase prepared from Phanerochaete chrysosporium - A white rot fungus. *Chemosphere* **2009**, *75* (8), 1003−1007.

(15) Shen, M.; Huang, Z.; Luo, X.; et al. Activation of persulfate for tetracycline degradation using the catalyst regenerated from Fenton sludge containing heavy metal: Synergistic effect of Cu for catalysis. *Chem. Eng. J.* **2020**, *396*, No. 125238.

(16) Zhu, X.; Yuan, W.; Lang, M.; Zhen, G.; Zhang, X.; Lu, X. Novel methods of sewage sludge utilization for photocatalytic degradation of tetracycline-containing wastewater. *Fuel* **2019**, *252*, 148−156.

(17) Shen, M.; Huang, Z.; Qiu, L.; et al. Recycling of Fenton sludge containing Ni as an efficient catalyst for tetracycline degradation through peroxymonosulfate activation. *J. Cleaner Prod.* **2020**, *268*, No. 122174.

(18) Luo, X.; Shen, M.; Liu, J.; et al. Resource utilization of piggery sludge to prepare recyclable magnetic biochar for highly efficient degradation of tetracycline through peroxymonosulfate activation. *J. Cleaner Prod.* **2021**, *294*, No. 126372.

(19) Wei, J.; Liu, Y.; Zhu, Y.; Li, J. Enhanced catalytic degradation of tetracycline antibiotic by persulfate activated with modified sludge bio-hydrochar. *Chemosphere* **2020**, *247*, No. 125854.

(20) Ledjeri, A.; Yahiaoui, I.; Aissani-Benissad, F. The electro/Fe 3+ /peroxydisulfate (PDS) process coupled to activated sludge culture for the degradation of tetracycline. *J. Environ. Manage.* **2016**, *184*, 249−254.

(21) Yang, G.; Gao, Q.; Yang, S.; et al. Strong adsorption of tetracycline hydrochloride on magnetic carbon-coated cobalt oxide nanoparticles. *Chemosphere* **2020**, *239*, No. 124831.

(22) Liu, Y.; Liu, H.; Zhou, Z.; Wang, T.; Ong, C. N.; Vecitis, C. D. Degradation of the Common Aqueous Antibiotic Tetracycline using a Carbon Nanotube Electrochemical Filter. *Environ. Sci. Technol.* **2015**, *49* (13), 7974−7980.

(23) Chen, Y. Y.; Ma, Y. L.; Yang, J.; Wang, L. Q.; Lv, J. M.; Ren, C. J. Aqueous tetracycline degradation by H2O2 alone: Removal and transformation pathway. *Chem. Eng. J.* **2017**, *307*, 15−23.

(24) Zhi, D.; Wang, J.; Zhou, Y.; et al. Development of ozonation and reactive electrochemical membrane coupled process: Enhanced tetracycline mineralization and toxicity reduction. *Chem. Eng. J.* **2020**, *383*, No. 123149.

(25) Zhong, S. F.; Yang, B.; Xiong, Q.; Cai, W. W.; Lan, Z. G.; Ying, G. G. Hydrolytic transformation mechanism of tetracycline antibiotics: Reaction kinetics, products identification and determination in WWTPs. *Ecotoxicol. Environ. Saf.* **2022**, *229*, No. 113063.

(26) Wu, P.-H.; Li, Y.; Wu, P.-H.; Yu, C.-P. Microbial fuel cell-driven alkaline thermal hydrolysis for pretreatment of wastewater containing high concentrations of tetracycline in the cathode chamber. *J. Environ. Chem. Eng.* **2021**, *9* (1), No. 104659.

(27) Yi, Q.; Gao, Y.; Zhang, H.; Zhang, H.; Zhang, Y.; Yang, M. Establishment of a pretreatment method for tetracycline production wastewater using enhanced hydrolysis. *Chem. Eng. J.* **2016**, *300*, 139−145.

(28) Ahmadi, M.; Ramezani Motlagh, H.; Jaafarzadeh, N.; et al. Enhanced photocatalytic degradation of tetracycline and real pharmaceutical wastewater using MWCNT/TiO2 nano-composite. *J. Environ. Manage.* **2017**, *186*, 55−63.

(29) Bui, T. S.; Bansal, P.; Lee, B. K.; Mahvelati-Shamsabadi, T.; Soltani, T. Facile fabrication of novel Ba-doped g-C3N4 photocatalyst with remarkably enhanced photocatalytic activity towards tetracycline elimination under visible-light irradiation. *Appl. Surf. Sci.* **2020**, *506*, No. 144184.

(30) Liu, B.; Song, W.; Zhang, W.; et al. Fe3O4@CNT as a high-effective and steady chainmail catalyst for tetracycline degradation with peroxydisulfate activation: Performance and mechanism. *Sep. Purif. Technol.* **2021**, *273*, No. 118705.

(31) Meng, Z.; Mo, R.; Wang, Q.; Zheng, K.; Li, W.; Qin, C. Nitrogen-doped porous carbon derived from graphite of solid waste for activating peroxymonosulfate to degradation tetracycline. *Colloids Surf., A* **2023**, *662*, No. 130984.

(32) Sun, X.; Wang, G.; Huang, L.; et al. Microwave-assisted co-precipitation preparation of CuFe2O4 photo-Fenton degradation tetracycline: Characterization, efficacy, stability in complex water quality and mechanism. *J. Environ. Chem. Eng.* **2023**, *11* (1), No. 109164.

(33) Baladi, E.; Davar, F.; Hojjati-Najafabadi, A. Synthesis and characterization of g−C3N4−CoFe2O4−ZnO magnetic nanocomposites for enhancing photocatalytic activity with visible light for degradation of penicillin G antibiotic. *Environ. Res.* **2022**, *215*, No. 114270.

(34) Hojjati-Najafabadi, A.; Aygun, A.; Tiri, R. N. E.; et al. Bacillus thuringiensis Based Ruthenium/Nickel Co-Doped Zinc as a Green Nanocatalyst: Enhanced Photocatalytic Activity, Mechanism, and Efficient H2 Production from Sodium Borohydride Methanolysis. *Ind. Eng. Chem. Res.* **2023**, *62* (11), 4655−4664.

(35) Kumar, G.; Mukherjee, I.; Dubey, M.; Vellenki, B. P.; Dutta, R. K. Photocatalytic degradation of tetracycline in aqueous medium using ZnWO4/Bi2MoO6 nanocomposites under natural sunlight. *Int. J. Environ. Sci. Technol.* **2023**, *20* (3), 2903−2918.

(36) Oluwole, A. O.; Olatunji, O. S. Photocatalytic degradation of tetracycline in aqueous systems under visible light irridiation using needle-like SnO2 nanoparticles anchored on exfoliated g-C3N4. *Environ. Sci. Eur.* **2022**, *34* (1), No. 5.

(37) Nie, M.; Li, Y.; He, J.; et al. Degradation of tetracycline in water using Fe3O4 nanospheres as Fenton-like catalysts: Kinetics, mechanisms and pathways. *New J. Chem.* **2020**, *44* (7), 2847−2857.

(38) Wang, S.; Zhao, L.; Huang, W.; et al. Solvothermal synthesis of CoO/BiVO4 p-n heterojunction with micro-nano spherical structure for enhanced visible light photocatalytic activity towards degradation of tetracycline. *Mater. Res. Bull.* **2021**, *135*, No. 111161.

(39) Soltani, R. D. C.; Mashayekhi, M.; Naderi, M.; Boczkaj, G.; Jorfi, S.; Safari, M. Sonocatalytic degradation of tetracycline antibiotic using zinc oxide nanostructures loaded on nano-cellulose from waste straw as nanosonocatalyst. *Ultrason. Sonochem.* **2019**, *55*, 117−124.

(40) Liu, Z.; Zhu, M.; Zhao, L.; et al. Aqueous tetracycline degradation by coal-based carbon electrocatalytic filtration mem-

brane: Effect of nano antimony-doped tin dioxide coating. *Chem. Eng. J.* **2017**, *314*, 59−68.

(41) Jiang, X.; Guo, Y.; Zhang, L.; Jiang, W.; Xie, R. Catalytic degradation of tetracycline hydrochloride by persulfate activated with nano Fe0 immobilized mesoporous carbon. *Chem. Eng. J.* **2018**, *341*, 392−401.

(42) Cao, P.; Zhang, Y.; Gao, D.; et al. Constructing nano-heterojunction of MOFs with crystal regrowth for efficient degradation of tetracycline under visible light. *J. Alloys Compd.* **2022**, *904*, No. 164061.

(43) Liu, Z.; Zhu, M.; Wang, Z.; Wang, H.; Deng, C.; Li, K. Effective degradation of aqueous tetracycline using a nano-TiO2/carbon electrocatalytic membrane. *Materials* **2016**, *9* (5), 364.

(44) Wang, Y.; Qiang, Z.; Zhu, W.; et al. BiPO 4 Nanorod/Graphene Composite Heterojunctions for Photocatalytic Degradation of Tetracycline Hydrochloride. *ACS Appl. Nano Mater.* **2021**, *4* (9), 8680−8689.

(45) Jia, D.; Zhang, Y.; Zhang, X.; et al. Facile fabrication of Bi nanoparticle-decorated g-C3N4photocatalysts for effective tetracy-cline hydrochloride degradation: environmental factors, degradation mechanism, pathways and biotoxicity evaluation. *Environ. Sci.: Nano* **2021**, *8* (2), 415−431.

(46) Gu, W.; Li, Q.; Zhu, H.; Zou, L. Facile interface engineering of hierarchical flower spherical-like Bi-metal−organic framework micro-sphere/Bi2MoO6 heterostructure for high-performance visible−light photocatalytic tetracycline hydrochloride degradation. *J. Colloid Interface Sci.* **2022**, *606*, 1998−2010.

(47) Fiaz, A.; Zhu, D.; Sun, J. Environmental fate of tetracycline antibiotics: degradation pathway mechanisms, challenges, and perspectives. *Environ. Sci. Eur.* **2021**, *33* (1), No. 64.

(48) Jodeyri, M.; Haghighi, M.; Shabani, M. Enhanced-photo-reduction deposition of Ag over sono-dispersed C3N4-Clinoptilolite used as nanophotocatalyst for efficient photocatalytic degradation of tetracycline antibiotic under simulated solar-light. *J. Mater. Sci.: Mater. Electron.* **2019**, *30* (15), 13877−13894.

(49) Li, Z.; Ma, H.; Zang, L.; Li, D.; Guo, S.; Shi, L. Construction of nano-flower MIL-125(Mo)-In2Se3 Z-scheme heterojunctions by one-step solvothermal method for removal of tetracycline from wastewater in the synergy of adsorption and photocatalysis way. *Sep. Purif. Technol.* **2021**, *276*, No. 119355.

(50) Wang, X.; Zhang, B.; Ma, J.; Ning, P. Novel synthesis of aluminum hydroxide gel-coated nano zero-valent iron and studies of its activity in flocculation-enhanced removal of tetracycline. *J. Environ. Sci.* **2020**, *89*, 194−205.

(51) Jiang, Y.; Peng, Z.; Wu, F.; et al. A novel 3D/2D CdIn2S4 nano-octahedron/ZnO nanosheet heterostructure: Facile synthesis, synergistic effect and enhanced tetracycline hydrochloride photo-degradation mechanism. *Dalton Trans.* **2018**, *47* (26), 8724−8737.

(52) Guo, S.; Luo, H.; Li, Y.; et al. Structure-controlled three-dimensional BiOI/MoS2 microspheres for boosting visible-light photocatalytic degradation of tetracycline. *J. Alloys Compd.* **2021**, *852*, No. 157026.

(53) Shi, Z.; Zhang, Y.; Duoerkun, G.; et al. Fabrication of MoS2/BiOBr heterojunctions on carbon fibers as a weaveable photocatalyst for tetracycline hydrochloride degradation and Cr(vi) reduction under visible light. *Environ. Sci.: Nano* **2020**, *7* (9), 2708−2722.

(54) Hou, X.; Shi, J.; Wang, N.; et al. Removal of antibiotic tetracycline by metal-organic framework MIL-101(Cr) loaded nano zero-valent iron. *J. Mol. Liq.* **2020**, *313*, No. 113512.

(55) Meng, F.; Ma, W.; Wang, Y.; Zhu, Z.; Chen, Z.; Lu, G. A tribo-positive Fe@MoS2 piezocatalyst for the durable degradation of tetracycline: degradation mechanism and toxicity assessment. *Environ. Sci.: Nano* **2020**, *7* (6), 1704−1718.

(56) Wang, X.; Xie, Y.; Ma, J.; Ning, P. Facile assembly of novel g-C3N4@expanded graphite and surface loading of nano zero-valent iron for enhanced synergistic degradation of tetracycline. *RSC Adv.* **2019**, *9* (59), 34658−34670.

(57) Sharma, S. K.; Kumar, A.; Sharma, G.; et al. LaTiO2N/Bi2S3 Z-scheme nano heterostructures modified by rGO with high

interfacial contact for rapid photocatalytic degradation of tetracycline. *J. Mol. Liq.* **2020**, *311*, No. 113300.

(58) Zhang, K.; Gu, S.; Wu, Y.; Fan, Q.; Zhu, C. Preparation of pyramidal SnO/CeO2 nano-heterojunctions with enhanced photo-catalytic activity for degradation of tetracycline. *Nanotechnology* **2020**, *31* (21), No. 215702.

(59) Li, X.; Xiong, J.; Gao, X.; et al. Novel BP/BiOBr S-scheme nano-heterojunction for enhanced visible-light photocatalytic tetracy-cline removal and oxygen evolution activity. *J. Hazard Mater.* **2020**, *387*, No. 121690.

(60) Ma, Z.; Hu, L.; Li, X.; Deng, L.; Fan, G.; He, Y. A novel nano-sized MoS2 decorated Bi2O3 heterojunction with enhanced photo-catalytic performance for methylene blue and tetracycline degrada-tion. *Ceram. Int.* **2019**, *45* (13), 15824−15833.

(61) Nasseh, N.; Barikbin, B.; Taghavi, L. Photocatalytic degradation of tetracycline hydrochloride by FeNi3/SiO2/CuS magnetic nano-composite under simulated solar irradiation: Efficiency, stability, kinetic and pathway study. *Environ. Technol. Innovation* **2020**, *20*, No. 101035.

(62) Xu, J.; Zhang, B.; Jia, L.; Bi, N.; Zhao, T. Metal-enhanced fluorescence detection and degradation of tetracycline by silver nanoparticle-encapsulated halloysite nano-lumen. *J. Hazard Mater.* **2020**, *386*, No. 121630.

(63) Majumdar, A.; Ghosh, U.; Pal, A. Novel 2D/2D g-C3N4/Bi4NbO8Cl nano-composite for enhanced photocatalytic degradation of oxytetracycline under visible LED light irradiation. *J. Colloid Interface Sci.* **2021**, *584*, 320−331.

(64) Nasseh, N.; Hossein Panahi, A.; Esmati, M.; et al. Enhanced photocatalytic degradation of tetracycline from aqueous solution by a novel magnetically separable FeNi3/SiO2/ZnO nano-composite under simulated sunlight: Efficiency, stability, and kinetic studies. *J. Mol. Liq.* **2020**, *301*, No. 112434.

(65) Sun, R.; Yang, J.; Huang, R.; Wang, C. Controlled carbonization of microplastics loaded nano zero-valent iron for catalytic degradation of tetracycline. *Chemosphere* **2022**, *303*, No. 135123.

(66) Li, Z.; Guo, C.; Lyu, J.; Hu, Z.; Ge, M. Tetracycline degradation by persulfate activated with magnetic Cu/CuFe2O4 composite: Efficiency, stability, mechanism and degradation pathway. *J. Hazard Mater.* **2019**, *373*, 85−96.

(67) Tang, S.; Zhao, M.; Yuan, D.; et al. Fe3O4 nanoparticles three-dimensional electro-peroxydisulfate for improving tetracycline degra-dation. *Chemosphere* **2021**, *268*, No. 129315.

(68) Zhang, Y.; Xu, H.; Chen, M.; Chen, P.; Gou, G.; Chen, Y. Simultaneous adsorption and degradation tetracycline and heavy metals using polyaniline/chitosan to loading nanoscale zero-valent iron. *Phys. Chem. Liq.* **2022**, *60* (3), 351−368.

(69) Wang, J.; Li, P.; Zhao, Y.; Zeng, X. Nb/N Co-Doped Layered Perovskite Sr2TiO4: Preparation and Enhanced Photocatalytic Degradation Tetracycline under Visible Light. *Int. J. Mol. Sci.* **2022**, *23* (18), 10927.

(70) Xu, K.; Zhang, Q.; Xu, W.; Kang, X.; Wang, L. Er-doping g-C3N4/boron carbon nitride quantum dots composites under visible light irradiation for tetracycline degradation. *Mater. Lett.* **2022**, *311*, No. 131489.

(71) Balta, Z.; Simsek, E. B. Understanding the structural and photocatalytic effects of incorporation of hexagonal boron nitride whiskers into ferrite type perovskites (BiFeO3, MnFeO3) for effective removal of pharmaceuticals from real wastewater. *J. Alloys Compd.* **2022**, *898*, No. 162897.

(72) Zhang, G.; Chen, S.; Yang, Y.; et al. Boron nitride quantum dots decorated MIL-100(Fe) for boosting the photo-generated charge separation in photocatalytic refractory antibiotics removal. *Environ. Res.* **2021**, *202*, No. 111661.

(73) Xu, W.; Zhang, Q.; Xu, K.; Qiu, L.; Song, J.; Wang, L. Study on visible light photocatalytic performance of BiVO4 modified by graphene analogue boron nitride. *Chemosphere* **2022**, *307*, No. 135811.

(74) Du, Z.; Feng, L.; Guo, Z.; et al. Ultrathin h-BN/Bi2MoO6 heterojunction with synergetic effect for visible-light photocatalytic tetracycline degradation. *J. Colloid Interface Sci.* **2021**, *589*, 545−555.

(75) Han, T.; Chen, Y.; Shi, H. Construction of dual-channel charge transfer over Bi/BiOBr/BNQDs photocatalyst system toward boosting tetracycline degradation. *Surf. Interfaces* **2022**, *35*, No. 102402.

(76) Idrees, S. A.; Jamil, L. A.; Omer, K. M. Silver-Loaded Carbon and Phosphorous Co-Doped Boron Nitride Quantum Dots (Ag@CP-BNQDs) for Efficient Organic Waste Removal: Theoretical and Experimental Investigations. *ACS Omega* **2022**, *7* (42), 37620−37628.

(77) Yan, T.; Du, Z.; Wang, J.; et al. Construction of 2D/2D Bi2WO6/BN heterojunction for effective improvement on photocatalytic degradation of tetracycline. *J. Alloys Compd.* **2022**, *894*, No. 162487.

(78) Guo, P.; Zhao, F.; Hu, X. Boron- and europium-co-doped g-C3N4 nanosheets: Enhanced photocatalytic activity and reaction mechanism for tetracycline degradation. *Ceram. Int.* **2021**, *47* (11), 16256−16268.

(79) Guo, P.; Zhao, F.; Hu, X. Fabrication of a direct Z-scheme heterojunction between MoS2 and B/Eu-g-C3N4 for an enhanced photocatalytic performance toward tetracycline degradation. *J. Alloys Compd.* **2021**, *867*, No. 159044.

(80) Gong, Y.; Liu, Y.; Cui, X.; et al. N/B co-doped polymeric carbon nitride with boosted charge transfer property and enhanced photocatalytic degradation of tetracycline. *Appl. Surf. Sci.* **2022**, *604*, No. 154655.

(81) Guo, Y.; Yan, C.; Guo, Y.; Ji, X. UV-light promoted formation of boron nitride-fullerene composite and its photodegradation performance for antibiotics under visible light irradiation. *J. Hazard. Mater.* **2021**, *410*, No. 124628.

(82) Ji, X.; Liu, X.; Guo, Y.; Zhang, J. Developing visible light responsive Z-scheme BN-PDI photocatalysts with good degradation performance for antibiotics. *Chem. Eng. J.* **2021**, *425*, No. 131260.

(83) Shen, Q.; Wei, L.; Bibi, R.; et al. Boosting photocatalytic degradation of tetracycline under visible light over hierarchical carbon nitride microrods with carbon vacancies. *J. Hazard Mater.* **2021**, *413*, No. 125376.

(84) Xu, K.; Zhang, Q.; Wang, C.; et al. 0D boron carbon nitride quantum dots decorated 2D Bi4O5I2 as 0D/2D efficient visible-light-driven photocatalysts for tetracyclines photodegradation. *Chemosphere* **2022**, *289*, No. 133230.

(85) Wang, M.; Wang, J.; Li, M.; Wang, X.; Sima, Y.; Wu, Q. Novel In2S3/Zn−Al LDHs composite as an efficient visible-light-driven photocatalyst for tetracycline degradation. *Opt. Mater.* **2022**, *128*, No. 112376.

(86) Chakraborty, K.; Pal, T.; Ghosh, S. RGO-ZnTe: A Graphene Based Composite for Tetracycline Degradation and Their Synergistic Effect. *ACS Appl. Nano Mater.* **2018**, *1* (7), 3137−3144.

(87) Chen, F.; Yang, Q.; Li, X.; et al. Hierarchical assembly of graphene-bridged Ag3PO4/Ag/BiVO4 (040) Z-scheme photocatalyst: An efficient, sustainable and heterogeneous catalyst with enhanced visible-light photoactivity towards tetracycline degradation under visible light irradiation. *Appl. Catal., B* **2017**, *200*, 330−342.

(88) Wang, C.; Li, S.; Cai, M.; et al. Rationally designed tetra (4-carboxyphenyl) porphyrin/graphene quantum dots/bismuth molybdate Z-scheme heterojunction for tetracycline degradation and Cr(VI) reduction: Performance, mechanism, intermediate toxicity appraisement. *J. Colloid Interface Sci.* **2022**, *619*, 307−321.

(89) Wang, K.; Zhan, S.; Zhang, D.; Sun, H.; Jin, X.; Wang, J. In situ grown monolayer N−Doped graphene and ZnO on ZnFe2O4 hollow spheres for efficient photocatalytic tetracycline degradation. *Colloids Surf., A* **2021**, *618*, No. 126362.

(90) Liu, L.; Yu, M.; Li, Y.; et al. Microwave (MW)-assisted design of cobalt anchored 2D graphene-like carbon nanosheets (Co@GCNs) as peroxymonosulfate activator for tetracycline degradation and insight into the catalytic mechanism. *Sep. Purif. Technol.* **2022**, *295*, No. 121358.

(91) Huang, C.; Li, M.; Wang, P.; et al. Tetracycline degradation by persulfate activated with nitrogen magnetic graphene oxide confined Fe/Co dual single-atom catalyst: Performance and degradation mechanism. *J. Environ. Chem. Eng.* **2023**, *11* (3), No. 109704.

(92) Hasanmashaei, H.; Nasrollahi, Z.; Ebrahimian Pirbazari, A.; Esmaeili Khalil Saraei, F.; Alimoradi, S.; Tabatabai-Yazdi, F.-S. Magnetic graphene oxide supported plasmonic nanoparticles as visible-light driven photocatalysts: Experimental study and artificial intelligent modelling for tetracycline degradation. *J. Alloys Compd.* **2023**, *960*, No. 170660.

(93) Chen, J.; Xiao, X.; Wang, Y.; Lu, M.; Zeng, X. Novel AgI/BiOBr/reduced graphene oxide Z-scheme photocatalytic system for efficient degradation of tetracycline. *J. Alloys Compd.* **2019**, *800*, 88−98.

(94) Li, C.; Hu, R.; Lu, X.; Bashir, S.; Liu, J. L. Efficiency enhancement of photocatalytic degradation of tetracycline using reduced graphene oxide coordinated titania nanoplatelet. *Catal. Today* **2020**, *350*, 171−183.

(95) Cherifi, Y.; Addad, A.; Vezin, H.; et al. PMS activation using reduced graphene oxide under sonication: Efficient metal-free catalytic system for the degradation of rhodamine B, bisphenol A, and tetracycline. *Ultrason. Sonochem.* **2019**, *52*, 164−175.

(96) Lu, M.; Dong, J.; Hu, M.; Cheng, G.; Lv, J. Perovskite LaMnO3 Composite Graphene Carbon Nitride g-C3N4 Improves the Photocatalytic Performance of Tetracycline Degradation. *Water* **2023**, *15* (8), 1627.

(97) Zhao, D.; Cai, C. Preparation of Bi 2 MoO 6 /Ti 3 C 2 MXene heterojunction photocatalysts for fast tetracycline degradation and Cr(vi) reduction. *Inorg. Chem. Front* **2020**, *7* (15), 2799−2808.

(98) Shen, J.; Shen, J.; Zhang, W.; et al. Built-in electric field induced CeO2/Ti3C2-MXene Schottky-junction for coupled photocatalytic tetracycline degradation and CO2 reduction. *Ceram. Int.* **2019**, *45* (18), 24146−24153.

(99) Guan, Y.; Cao, Y.; Ma, S.; et al. Metal-free g-C3N5 photocatalyst coupling MXenes Ti3C2 for tetracycline degradation: Insight for electron transfer mechanism, degradation mechanism and photothermal effect. *J. Alloys Compd.* **2023**, *951*, No. 169864.

(100) Bao, Y.; Liu, Y.; Zhang, Z.; et al. Constructing 2D/2D ultrathin Ti3C2/SnS2 Schottky heterojunctions toward efficient tetracycline degradation. *Chemosphere* **2022**, *307*, No. 136118.

(101) Yue, R.; Sun, X. A Self-cleaning, catalytic titanium carbide (MXene) membrane for efficient tetracycline degradation through peroxymonosulfate activation: Performance evaluation and mechanism study. *Sep. Purif. Technol.* **2021**, *279*, No. 119796.

(102) Khanh Huyen, N. T.; Pham, T. D.; Dieu Cam, N. T.; et al. Fabrication of titanium doped BiVO4 as a novel visible light driven photocatalyst for degradation of residual tetracycline pollutant. *Ceram. Int.* **2021**, *47* (24), 34253−34259.

(103) Jiang, L.; et al. Doping of graphitic carbon nitride for photocatalysis: A review. *Appl. Catal., B* **2017**, *217*, 388−406.

(104) Duan, L.; Wang, B.; Heck, K. N.; et al. Titanium oxide improves boron nitride photocatalytic degradation of perfluorooctanoic acid. *Chem. Eng. J.* **2022**, *448*, No. 137735.

(105) Gunasekaran, S.; Seshadri, S.; Muthu, S.; Kumaresan, S.; Arunbalaji, R. Vibrational spectroscopy investigation using ab initio and density functional theory on p-anisaldehyde. *Spectrochim. Acta, Part A* **2008**, *70* (3), 550−556.

(106) Liu, Z.; Lu, T.; Chen, Q. An sp-hybridized all-carboatomic ring, cyclo[18]carbon: Electronic structure, electronic spectrum, and optical nonlinearity. *Carbon* **2020**, *165*, 461−467.

(107) Gber, T. E.; Louis, H.; Owen, A. E.; et al. Heteroatoms (Si, B, N, and P) doped 2D monolayer MoS2 for NH3 gas detection. *RSC Adv.* **2022**, *12* (40), 25992−26010.

(108) Chen, Y.; Xu, D.; Zhang, S.; Tan, R.; Li, L.; Liu, X. Density functional theory calculations on the adsorption and degradation characteristics of ronidazole on the TiO2 surface. *Int. J. Quantum Chem.* **2021**, *121* (13), No. e26648. DOI: 10.1002/qua.26648.

(109) Elkholy, A. E.; El-Taib Heakal, F.; Rashad, A. M.; Zakaria, K. Monte Carlo simulation for guar and xanthan gums as green scale inhibitors. *J. Pet Sci. Eng.* **2018**, *166*, 263−273.

(110) Elkholy, A. E.; Rizk, S. A.; Rashad, A. M. Enhancing lubricating oil properties using novel quinazolinone derivatives: DFT study and molecular dynamics simulation. *J. Mol. Struct.* **2019**, *1175*, 788−796.

(111) Louis, H.; Isang, B. B.; Unimuke, T. O.; et al. Modeling of Al12N12, Mg12O12, Ca12O12, and C23N nanostructured as potential anode materials for sodium-ion battery. *J. Solid State Electrochem.* **2023**, *27* (1), 47−59.

(112) Guo, J.; Zhang, Y. Reactive Molecular Dynamics Simulation on Degradation of Tetracycline Antibiotics Treated by Cold Atmospheric Plasmas. *Molecules* **2023**, *28* (9), 3850.

(113) Foo, K. Y.; Hameed, B. H. Insights into the modeling of adsorption isotherm systems. *Chem. Eng. J.* **2010**, *156* (1), 2−10.

(114) Montemore, M. M.; van Spronsen, M. A.; Madix, R. J.; Friend, C. M. O2 Activation by Metal Surfaces: Implications for Bonding and Reactivity on Heterogeneous Catalysts. *Chem. Rev.* **2018**, *118* (5), 2816−2862.

(115) Zang, Y.; Zhou, M.; Wu, Y.; Qin, S.; Huang, S.; Meng, J. Numerical Simulation of Interaction between Plasma and Azithromycin Based on Molecular Dynamics. *Appl. Sci.* **2022**, *12* (24), 12878.

(116) Al-zaqri, N.; Pooventhiran, T.; Rao, D. J.; Alsalme, A.; Warad, I.; Thomas, R. Structure, conformational dynamics, quantum mechanical studies and potential biological activity analysis of multiple sclerosis medicine ozanimod. *J. Mol. Struct.* **2021**, *1227*, No. 129685.

(117) Agwupuye, J. A.; Louis, H.; Unimuke, T. O.; David, P.; Ubana, E. I.; Moshood, Y. L. Electronic structure investigation of the stability, reactivity, NBO analysis, thermodynamics, and the nature of the interactions in methyl-substituted imidazolium-based ionic liquids. *J. Mol. Liq.* **2021**, *337*, No. 116458.

(118) Apebende, C. G.; Idante, P. S.; Louis, H.; et al. Integrated Spectroscopic, Bio-active Prediction and Analytics of Isoquinoline Derivative for Breast Cancer Mitigation. *Chemistry Africa* **2022**, *5* (6), 1979−1995.

(119) Sadeghi, S.; Mohammad Shiri, H.; Ehsani, A.; Oftadeh, M. Electrosynthesis of high-purity TbMn2O5 nanoparticles and its nanocomposite with conjugated polymer: Surface, density of state and electrochemical investigation. *Solid State Sci.* **2020**, *105*, No. 106227.

(120) Mohammadi, M. D.; Abdullah, H. Y.; Louis, H.; Etim, E. E.; Edet, H. O.; Godfrey, O. C. Hexachlorobenzene (HCB) adsorption onto the surfaces of C60, C59Si, and C59Ge: Insight from DFT, QTAIM, and NCI. *Chem. Phys. Impact* **2023**, *6*, No. 100234.

(121) Farrokhpour, H.; Jouypazadeh, H.; Vakili Sohroforouzani, S. Interaction of different types of nanocages (Al12N12, Al12P12, B12N12, Be12O12, Mg12O12, Si12C12 and C24) with HCN and ClCN: DFT, TD-DFT, QTAIM, and NBO calculations. *Mol. Phys.* **2020**, *118* (4), No. 1626506.

(122) Doust Mohammadi, M.; Abdullah, H. Y. Theoretical study of the adsorption of amantadine on pristine, Al-, Ga-, P-, and As-doped boron nitride nanosheets: a PBC-DFT, NBO, and QTAIM study. *Theor. Chem. Acc.* **2020**, *139* (10), No. 158.

(123) Louis, H.; Egemonye, T. C.; Unimuke, T. O.; et al. Detection of Carbon, Sulfur, and Nitrogen Dioxide Pollutants with a 2D Ca12O12 Nanostructured Material. *ACS Omega* **2022**, *7* (39), 34929−34943.

(124) Eno, E. A.; Louis, H.; Ekoja, P.; et al. Experimental and computational modeling of the biological activity of benzaldehyde sulphur trioxide as a potential drug for the treatment of Alzheimer disease. *J. Indian Chem. Soc.* **2022**, *99* (7), No. 100532.

(125) Mujafarkani, N.; Bassey, V.; Tokono, J. J.; et al. Synthesis, characterization, and molecular modeling of phenylenediamine-phenylhydrazine-formaldehyde terpolymer (PPHF) as potent anti-inflammatory agent. *Heliyon* **2023**, *9* (7), No. e18067.

(126) Zhang, N. N.; Li, J.; Xiao, H. The Key Role of Competition between Orbital and Electrostatic Interactions in the Adsorption on Transition Metal Single-Atom Catalysts Anchored by N-doped Graphene. *ChemCatChem* **2022**, *14* (16), No. e202200275, DOI: 10.1002/cctc.202200275.

(127) Matta, C. F. On the connections between the quantum theory of atoms in molecules (QTAIM) and density functional theory (DFT): a letter from Richard F. W. Bader to Lou Massa. *Struct Chem.* **2017**, *28* (5), 1591−1597.

(128) Jaziri, E.; Louis, H.; Gharbi, C.; et al. Synthesis, X-ray crystallography, molecular electronic property investigation, and leukopoiesis activity of novel 4,6-dimethyl-1,6-dihydropyridin-2-amino nitrate hybrid material. *J. Mol. Struct.* **2022**, *1268*, No. 133733.

(129) Ogunwale, G. J.; Louis, H.; Gber, T. E.; Adeyinka, A. S. Modeling of pristine, Ir- and Au-decorated C60 fullerenes as sensors for detection of hydroxyurea and nitrosourea drugs. *J. Environ. Chem. Eng.* **2022**, *10* (6), No. 108802.

(130) Hadi, Z.; Nouraliei, M.; Yousefi-Siavoshani, A.; Javadian, H.; Chalanchi, S. M.; Hashemi, S. S. A DFT study on the therapeutic potential of carbon nanostructures as sensors and drug delivery carriers for curcumin molecule: NBO and QTAIM analyses. *Colloids Surf., A* **2022**, *651*, No. 129698.

(131) Ogunwale, G. J.; Louis, H.; Unimuke, T. O.; et al. Interaction of 5-Fluorouracil on the Surfaces of Pristine and Functionalized Ca 12 O 12 Nanocages: An Intuition from DFT. *ACS Omega* **2023**, *8* (15), 13551−13568.

(132) Ali, I.; Faraz Ud Din, M.; Cuzzupè, D. T.; et al. Ti3C2Tx-Modified PEDOT:PSS Hole-Transport Layer for Inverted Perovskite Solar Cells. *Molecules* **2022**, *27* (21), 7452.

(133) Lu, T.; Chen, F. Multiwfn: A multifunctional wavefunction analyzer. *J. Comput. Chem.* **2012**, *33* (5), 580−592.

(134) Inah, B. E.; Louis, H.; Benjamin, I.; Unimuke, T. O.; Adeyinka, A. S. Computational study on the interactions of functionalized C24 NC (NC═C, − OH, − NH2, − COOH, and B) with chloroethylphenylbutanoic acid. *Can. J. Chem.* **2023**, *101* (1), 11−24.

(135) Louis, H.; Amodu, I. O.; Unimuke, T. O.; Gber, T. E.; Isang, B. B.; Adeyinka, A. S. Modeling of Ca12O12, Mg12O12, and Al12N12 nanostructured materials as sensors for phosgene (Cl2CO). *Mater. Today Commun.* **2022**, *32*, No. 103946.

(136) Bahamon, D.; Khalil, M.; Belabbes, A.; Alwahedi, Y.; Vega, L. F.; Polychronopoulou, K. A DFT study of the adsorption energy and electronic interactions of the SO2 molecule on a CoP hydrotreating catalyst. *RSC Adv.* **2021**, *11* (5), 2947−2957.

(137) Dou, X.; Keywanlu, M.; Tayebee, R.; Mahdavi, B. Simulation of adsorption and release of doxepin onto ZIF-8 including in vitro cellular toxicity and viability. *J. Mol. Liq.* **2021**, *329*, No. 115557.

(138) Liang, X.; Zhang, J.; Zhang, K.; Yang, X.; Zhang, M. The modification effect of Fe2O3 nanoparticles on ZnO nanorods improves the adsorption and detection capabilities of TEA. *Inorg. Chem. Front.* **2022**, *9* (2), 259−266.

(139) Zhihong, Y.; Ye, Y.; Pejhan, A.; Nasr, A. H.; Nourbakhsh, N.; Tayebee, R. A theoretical study on the pure and doped ZnO nanoclusters as effective nanobiosensors for 5-fluorouracil anticancer drug adsorption. *Appl. Organomet. Chem.* **2020**, *34* (4), No. e5534, DOI: 10.1002/aoc.5534.

(140) Hojjati-Najafabadi, A.; Nasr Esfahani, P.; Davar, F.; Aminabhavi, T. M.; Vasseghian, Y. Adsorptive removal of malachite green using novel GO@ZnO-NiFe2O4-αAl2O3 nanocomposites. *Chem. Eng. J.* **2023**, *471*, No. 144485.

(141) Dąbrowski, A. Adsorption — from theory to practice. *Adv. Colloid Interface Sci.* **2001**, *93* (1−3), 135−224.

(142) Ebelegi, A. N.; Ayawei, N.; Wankasi, D. Interpretation of Adsorption Thermodynamics and Kinetics. *Open J. Phys. Chem.* **2020**, *10* (03), 166−182.

(143) Yang, X.; Zhao, H.; Qu, Z.; et al. The effect of oxygen-containing functional groups on formaldehyde adsorption in solution on carbon surface: A density functional theory study. *J. Environ. Chem. Eng.* **2021**, *9* (5), No. 105987.

(144) Guo, T.; Jiang, L.; Wang, K.; et al. Efficient persulfate activation by hematite nanocrystals for degradation of organic

pollutants under visible light irradiation: Facet-dependent catalytic performance and degradation mechanism. *Appl. Catal., B* **2021**, *286*, No. 119883.

(145) Meng, F.; Ma, W.; Wang, Y.; Zhu, Z.; Chen, Z.; Lu, G. A tribo-positive Fe@MoS$_2$ piezocatalyst for the durable degradation of tetracycline: degradation mechanism and toxicity assessment. *Environ. Sci.: Nano* **2020**, *7* (6), 1704−1718.

(146) Chandana, S. N.; Al-Ostoot, F. H.; Eissa Mohammed, Y. H.; et al. Synthesis, structural characterization, and DFT studies of anti-cancer drug N-(2-Aminophenyl)-2-(4-bromophenoxy)acetamide. *Heliyon* **2021**, *7* (3), No. e06464.

(147) Udoikono, A. D.; Louis, H.; Eno, E. A.; et al. Reactive azo compounds as a potential chemotherapy drugs in the treatment of malignant glioblastoma (GBM): Experimental and theoretical studies. *J. Photochem. Photobiol.* **2022**, *10*, No. 100116.

(148) Owen, A. E.; Louis, H.; Agwamba, E. C.; Udoikono, A. D.; Manicum, A.-L. E. Antihypotensive potency of p-synephrine: Spectral analysis, molecular properties and molecular docking investigation. *J. Mol. Struct.* **2023**, *1273*, No. 134233.

(149) Zhang, Y.; Yuan, J.; Ding, Y.; Zhang, B.; Zhang, S.; Liu, B. Metal-free N-GQDs/P-g-C3N4 photocatalyst with broad-spectrum response: Enhanced exciton dissociation and charge migration for promoting H2 evolution and tetracycline degradation. *Sep. Purif. Technol.* **2023**, *304*, No. 122297.

(150) Wang, X.; Yu, Y.; Yang, C.; et al. Microfluidic 3D Printing Responsive Scaffolds with Biomimetic Enrichment Channels for Bone Regeneration. *Adv. Funct Mater.* **2021**, *31* (40), No. 2105190.

(151) Khan, M. U.; Mehboob, M. Y.; Hussain, R.; Afzal, Z.; Khalid, M.; Adnan, M. Designing spirobifullerene core based three-dimensional cross shape acceptor materials with promising photovoltaic properties for high-efficiency organic solar cells. *Int. J. Quantum Chem.* **2020**, *120* (22), No. e26377, DOI: 10.1002/qua.26377.

(152) Zhu, Y.; Zhao, F.; Wang, W.; Li, Y.; Zhang, S.; Lin, Y. Exciton Binding Energy of Non-Fullerene Electron Acceptors. *Adv. Energy Sustainability Res.* **2022**, *3* (4), No. 2100184.

(153) Aldrich, T. J.; Matta, M.; Zhu, W.; et al. Fluorination Effects on Indacenodithienothiophene Acceptor Packing and Electronic Structure, End-Group Redistribution, and Solar Cell Photovoltaic Response. *J. Am. Chem. Soc.* **2019**, *141* (7), 3274−3287.

(154) Hao, M.; Liu, T.; Xiao, Y.; et al. Achieving Balanced Charge Transport and Favorable Blend Morphology in Non-Fullerene Solar Cells via Acceptor End Group Modification. *Chem. Mater.* **2019**, *31* (5), 1752−1760.

(155) Wang, W.; Lu, H.; Chen, Z.; et al. High-performance NIR-sensitive fused tetrathienoacene electron acceptors. *J. Mater. Chem. A* **2020**, *8* (6), 3011−3017.